

# ~~Improving In Situ Monitoring of Seasonally Frozen Ground~~ ~~Monitoring Using Soil Freezing Characteristic Curve in~~ Permittivity-Temperature Space

Hesam Salmabadi<sup>1,2</sup>, Renato Pardo Lara<sup>3</sup>, Aaron Berg<sup>3</sup>, Alex Mavrovic<sup>1,2,4</sup>, Chelene Hanes<sup>5</sup>, Benoit Montpetit<sup>6</sup>, and Alexandre Roy<sup>1,2</sup>

<sup>1</sup>Department of Environmental Sciences, University of Quebec in Trois-Rivières, Trois-Rivières, Quebec, Canada

<sup>2</sup>Centre d'Études Nordiques, Université Laval, Québec, Quebec, Canada

<sup>3</sup>Department of Geography, Environment & Geomatics, University of Guelph, Guelph, Ontario, Canada

<sup>4</sup>Department of Physics, Cégep de Sherbrooke, Sherbrooke, Quebec, Canada

<sup>5</sup>Great Lakes Forestry Centre, Canadian Forest Service, Natural Resources Canada, Sault Ste. Marie, Ontario, Canada

<sup>6</sup>Climate Research Division, Environment and Climate Change Canada, Toronto, Ontario, Canada

**Correspondence:** Hesam Salmabadi (hesam.salmabadi@uqtr.ca)

**Abstract.** Frozen ground, a key indicator of climate change, profoundly influences ecological, hydrological, and carbon flux processes in cold regions. ~~However, traditional monitoring methods, which rely on a binary 0°C soil temperature threshold, fail to capture the complexities of soil freezing, such as freezing point depression and transitional states where water and ice coexist. This study introduces a framework that fits a theoretical Soil Freezing Characteristic Curve (SFCC) in permittivity-temperature~~  
5 ~~space to site- and cycle-specific~~ The Soil Freezing Characteristic Curve (SFCC), which defines the relationship between liquid water content and subzero temperatures, provides a framework for understanding soil freezing processes. However, accurately measuring liquid water content in frozen soils under field conditions remains challenging. We therefore recast an empirical SFCC model into permittivity-temperature space and fitted it to in situ measurements ~~. This approach enables the~~  
10 ~~quantification of the degree of soil freezing and the classification of soil states as frozen, unfrozen, or in transition (partially frozen). We analyzed 135 freezing cycles from from eight monitoring networks (87 sites, each equipped with permittivity-based soil moisture probes. These sites are part of eight monitoring networks spanning diverse Canadian landscapes, including eastern boreal forests (Montmorency Forest, La Romaine, James Bay, Chapleau), western boreal forests (Candle Lake), prairies (Kenaston sites) spanning Canadian boreal forests, prairies, and tundra ecozones, encompassing 96 freezing cycles measured with three sensor types (HydraProbe, TEROS12, and CS616). Using Bayesian hierarchical partial pooling, we~~  
15 ~~derived stabilized estimates of key SFCC parameters: the freezing onset temperature ( $T_f$ ) and the shape factor ( $b$ ), which controls transition sharpness. Network-level  $T_f$  ranged from 0.15 to 0.44°C, while  $b$  varied from 0.92 to 3.47 °C<sup>-1</sup>, reflecting distinct freezing regimes across ecozones. During the six-month freezing season (1 September–1 March), the James Bay (BJ), Montmorency Forest (FM), Chapleau (CP), and tundra regions (Trail Valley Creek and George River). On average, eastern boreal forest sites exhibited prolonged unfrozen and transitional states due to high soil moisture retention and insulation~~  
20 ~~from snow and vegetation cover (23 frozen days, 46 transitional days)~~ La Romaine (LR) networks, located in eastern boreal forests with thick organic layers and high moisture, remained predominantly unfrozen (70 days) or in transitional states (110

days) throughout winter despite persistent snow cover (> 90%) and subzero air temperatures. In contrast, western boreal forest sites experienced more extensive freezing under drier conditions (73 frozen days, 76 transitional days). Prairie sites displayed equal durations of frozen and transitional states (71 days each), while tundra sites had the longest frozen periods (145 frozen days, 52 transitional days). Notably, transitional periods lasted as long as—or even longer than—frozen ones, underscoring the limitations of binary classifications. Furthermore, the traditional 0°C threshold misclassified transitional soil states, overestimating frozen days by over 87% in prairie and western boreal regions, and unfrozen days by 86% in the eastern boreal forest. In tundra, the bias was more balanced, with 64% and 36% of transitional days misclassified as unfrozen and frozen, respectively. This SFCC-based framework enhances seasonally frozen ground monitoring, offering deeper insights into soil freeze-thaw dynamics. These advancements have implications for improving climate change assessments, refining carbon flux models, the Trail Valley Creek (TV) and training and validating remote sensing products. Additionally, the resulting database of soil states from this study provides a valuable resource for advancing frozen ground research, particularly in remote sensing and ecosystem modeling efforts. George River (GR) networks, located in tundra, exhibited prolonged frozen conditions (115 days) under extreme cold, though GR's higher moisture delayed freezing relative to TV under similar air temperature conditions. The Candle Lake (BT) network, located in western boreal forest, and the Kenaston (KN) network, located in prairies, showed intermediate responses, with BT experiencing 90 frozen and 30 transitional days, and KN averaging 70 frozen and 60 transitional days despite comparable air temperatures to the eastern boreal networks. These contrasting patterns reflect the combined effects of insulation layer such as snowpack, vegetation canopy, litter, and organic layers, together with moisture rather than air temperature alone, demonstrating how ground surface properties modulate soil thermal regimes. This framework provides a reproducible field-based approach to quantify seasonal surface soil freezing processes and a dataset for model and remote sensing evaluation.

## 1 Introduction

Frozen ground is defined as a condition in which pore water (the water inside the soil) turns into ice (Williams and Smith, 1989). Recognized as a key climate change indicator by the Environmental Protection Agency (EPA), this phenomenon is widespread and affects most land areas above 45°N latitude (Zhang et al., 2003). Frozen ground plays a major role in land surface energy and water balance, thereby impacting all ecological, hydrological, pedological, and biological activities in these regions (Ala-Aho et al., 2021; Hayashi, 2013; Ping et al., 2015; Loranty et al., 2018). By affecting hydrological partitioning, it regulates key processes such as infiltration, percolation, groundwater recharge, water chemistry, runoff characteristics, and evapotranspiration (Ala-Aho et al., 2021). Frozen ground impacts soil respiration, the primary pathway of carbon emissions to the atmosphere, as it is largely regulated by soil temperature and water content (Davidson and Janssens, 2006; Lei et al., 2022; Nikrad et al., 2016; Arndt et al., 2023; Azizi-Rad et al., 2022; Mikan et al., 2002; Mavrovic et al., 2023). Therefore, understanding frozen ground—its timing, extent, and duration—is critical for tracking climate change impacts and predicting changes in these vital environmental processes.

Beyond air temperature, which governs convective heat loss, soil freezing is primarily regulated by ground surface cover including snowpack, vegetation canopy and litter, moss, and organic (humus) layers as well as by soil moisture (MacKinney, 1929). Collectively, ground surface cover act as a thermal buffer, moderating soil–atmosphere heat exchange, conserving water, and reducing frost penetration (Fu et al., 2018). The insulating influence of snow, vegetation, litter, moss, and organic layers on soil temperature and moisture retention is well documented (Zhang, 2005; Decker et al., 2003; Flerchinger and Pierson, 1991; MacKinney, 1929). Meanwhile, moisture exerts a dual control: its latent heat delays freezing onset, whereas ice formation increases thermal conductivity and accelerates subsequent cooling (Kersten, 1949; Lei et al., 2020).

Traditionally, the state of the soil has been defined through a single measurement of soil temperature within the top few centimeters of the ground (Andersland and Ladanyi, 2003). Soil is labeled as frozen if the soil (or air temperature) is below 0°C and unfrozen if above. This approach is widely used in numerous studies, particularly in remote sensing, to monitor seasonally frozen ground conditions (Kim et al., 2011; Taghipourjavi et al., 2024; Zhang and Armstrong, 2001; Gao et al., 2020; Kou et al., 2017). However, the soil freezing and thawing process is not binary, using a single threshold of 0°C—the freezing point of pure water—is not sufficiently accurate (Pardo Lara et al., 2020; Mavrovic et al., 2020). In natural environments, soil typically begins to freeze at temperatures below 0°C (Dobiński, 2020), a phenomenon known as freezing point depression, which occurs due to adsorption, capillary action, adhesive and cohesive forces, and osmotic effects (Tian et al., 2014; Bouyoucos and McCool, 1915). Moreover, freezing occurs over a range of temperatures due to the presence of various types of water in the soil—hygroscopic (unfreezable) water, capillary water, water in soil pores, and gravitational water—all of which behave differently during freezing. This diversity creates a transitional zone where water and ice coexist, challenging the traditional binary classification (Tian et al., 2014; Zhang et al., 2019; Bouyoucos and McCool, 1915). Considering soil freezing point depression, rather than 0°C threshold, would enhance the accuracy of detecting the soil’s state, thereby minimizing false positives and negatives in assessments. Additionally, detecting the transitional period is crucial for accurately determining “zero curtain” periods. The zero curtain, observed during shoulder seasons, is a phase when soil temperatures hover around the soil’s freezing point regardless of air temperatures. This period is critical as the soil’s near-freezing temperature sustains microbial activity (Schimel and Mikan, 2005), significantly impacting carbon dioxide fluxes (Arndt et al., 2023). Studies show that carbon emissions during the zero curtain in the fall can match or exceed those of the rest of winter (Arndt et al., 2023; Mavrovic et al., 2023). Furthermore, an observed increase in the duration of the zero curtain period extending into the fall and winter seasons leads to higher carbon emissions during the non-growing season, underscoring the importance of accurately identifying these periods (Arndt et al., 2023).

The Soil Freezing/Thawing Characteristic Curve (SFCC/STCC), which defines the relationship between liquid water content ( $\theta_{lw}$ ) and subzero temperatures (Spaans and Baker, 1996; Koopmans and Miller, 1966), offers a framework for capturing the complexities of the soil freezing and thawing process (Pardo Lara et al., 2020). A typical SFCC/STCC (Fig. 1) consists of three zones (Zhang et al., 2019). Zone 1, called the “unfrozen zone,” occurs when the soil temperature is above the freezing point. In this zone, the pore water content remains almost constant, regardless of temperature changes. Zone 2, which starts immediately after the freezing point ( $T_f$ ), is the “transitional zone.” Here, there is a sharp decrease in pore water content as the soil-water system reaches a balance between liquid water  $\theta_{lw}$  and ice. Zone 3 begins at the soil temperature where the liquid

~~water content~~  $\theta_{lw}$  stabilizes, referred to as  $T_{res}$  (Kozłowski, 2007; Chen et al., 2021). In this zone, both bulk and capillary water content drop to zero, and the remaining water exists as a thin film bound to soil particles, commonly called unfreezable or bound water (Chen et al., 2021). The presence and behavior of  $\theta_{lw}$ , and consequently the shape of the SFCC, are influenced by numerous interrelated factors, including soil mineral composition, particle size, plasticity, initial water content, dry density, solute concentration, freezing rate, confining stress, and freeze-thaw history (Chai et al., 2018; Bi et al., 2023a, b, and references therein). The  $T_f$  decreases as initial water content decreases. For example, Zhang et al. (2019) found that decreasing soil water content from 37.60% to 14.52% lowered  $T_f$  from  $-0.06^\circ\text{C}$  to  $-0.75^\circ\text{C}$ . Soil texture also influences the SFCC. Fine-grained soils show greater freezing point depression and gradual changes in  $\theta_{lw}$ , while coarse-grained soils exhibit rapid water loss during freezing (Tian et al., 2014; Zhang et al., 2019; Bi et al., 2023b). Additionally, the freezing rate, by altering pore ice formation dynamics, solute distribution, and ice grain size, can affect both the slope and curvature of the SFCC (Watanabe and Osada, 2017). To construct the SFCC, measurements of ~~liquid water content~~  $\theta_{lw}$  and soil temperature are required. While measuring soil temperature is relatively straightforward, accurately quantifying the ~~liquid water content~~  $\theta_{lw}$  in frozen soil poses significant challenges, especially under field conditions. The hysteresis between SFCC and STCC has been widely documented, particularly under laboratory conditions (Wu et al., 2017; Mavrovic et al., 2020; Pardo Lara et al., 2020). In situ studies, such as Tomašková and In, reported approximately 10% higher unfrozen water content during freezing than during thawing at equivalent temperatures under saturated, fine-grained permafrost conditions, reflecting latent heat effects, cryosuction, and slow pore-water redistribution. Similarly, Overduin et al. (2006) documented asymmetric freezing–thawing transitions in saturated silty clays caused by latent heat and moisture migration. By contrast, near-surface, non-permafrost measurements found hysteresis to be theoretically expected but generally weak or indistinguishable (Pardo Lara et al., 2020).

Dielectric-based methods, such as Time Domain Reflectometry, Capacitance, and Impedance techniques, are widely used to estimate  $\theta_{lw}$  due to their ability to provide continuous, non-destructive in situ measurements (Seyfried and Murdock, 1996; Michael W Smith and Tice, 1988). These methods exploit the high permittivity contrast between liquid water ( $\epsilon_{lw} \approx 80$ ) and other soil components—air ( $\epsilon_{air} \approx 1$ ) and soil minerals ( $\epsilon_{soil} \approx 5$ )—allowing for efficient estimation of  $\theta_{lw}$ . Typically, physically based models, such as dielectric mixing models, or empirical models are employed to relate soil effective (bulk) permittivity ( $\epsilon_{eff}$ ), measured by dielectric probes—which represents the combined dielectric response of soil components—to  $\theta_{lw}$ . However, relating  $\epsilon_{eff}$  to  $\theta_{lw}$  in frozen soils remains challenging. Dielectric mixing models require accurate ice content estimates, which are difficult to obtain in situ, often leading to overestimations of  $\theta_{lw}$  when the ice component is neglected (Amankwah et al., 2022; Zhou et al., 2014; He and Dyck, 2013). This overestimation occurs because frozen soils, at identical liquid water contents, exhibit a higher  $\epsilon_{eff}$  than unfrozen soils due to the higher permittivity of ice ( $\epsilon_{r_{ice}} \approx 3.2 \epsilon_{ice} \approx 3.2$ ) compared to air ( $\epsilon_{r_{air}} \approx 1 \epsilon_{air} \approx 1$ ) (Spaans and Baker, 1995). Similarly, empirical models often rely on calibrations developed for unfrozen soils, limiting their applicability to frozen conditions (Yoshikawa and Overduin, 2005; He and Dyck, 2013). Calibration equations specifically developed for frozen soils are often restricted to saturated soils (Michael W Smith and Tice, 1988) or specific soil types, requiring prior knowledge of the soil's total water content before freezing (Spaans and Baker, 1995). These limitations make constructing the SFCC problematic, particularly in dynamic field environments. To address this, we constructed the SFCC directly in permittivity–temperature space, bypassing the need to estimate  $\theta_{lw}$ . ~~This approach improves the accuracy of~~

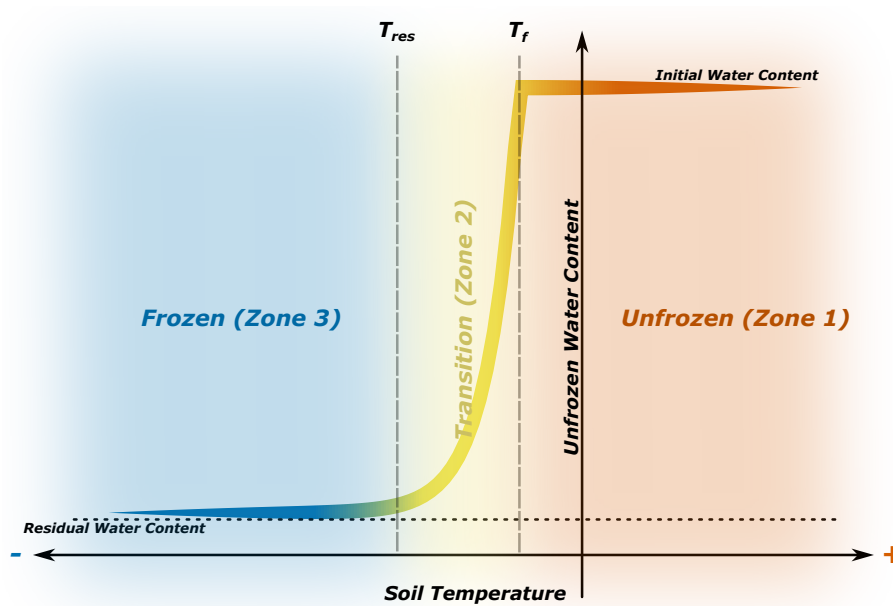


**Figure 1.** A typical Soil Freezing/Thawing Characteristic Curve (SFCC/STCC), adapted from Zhang et al. (2019).  $T_f$  marks the temperature at which soil begins to freeze, while  $T_{res}$  indicates the temperature at which the liquid water content stabilizes, nearly equal to the residual water content.

freeze–thaw characterization while overcoming the shortcomings of previous studies, which used logistic curve fitting with limited physical interpretability and robustness (Pardo Lara et al., 2020).

This study aims to enhance seasonally frozen ground monitoring by utilizing an SFCC model in the permittivity–temperature space. In this study, we apply the SFCC directly in permittivity–temperature space. By fitting this model to in situ measurements across diverse Canadian ecosystems—including prairies, to monitor seasonally frozen ground across 87 sites in eight Canadian monitoring networks spanning boreal forests, prairies, and tundra ecozones, with temporal coverage ranging from one to multiple years. Using measurements from three widely deployed sensor types (HydraProbe, TEROS12, and tundra regions—and constructing site- and cycle-specific SFCCs, we examine freezing and thawing processes in soils and define soil states under varying properties and climatic conditions. This work lays the foundation for improving remote sensing algorithms and ecosystem models, offering a more nuanced representation of soil state transitions beyond traditional binary approaches. CS616), we derive hourly soil freezing probabilities and investigate how freezing dynamics vary across networks.

## 2 Materials and Methods

### 2.1 Overview of Methodology

Before detailing the materials and methods, we provide an overview of the process. First, in situ data were collected (Sect. 2.1) and preprocessed (Sect. 2.2) to identify individual freezing and thawing cycles at each site. The SFCC model was then fitted (Sect. 2.3) to in situ soil temperature and  $\varepsilon_{\text{eff}}$  data using curve fitting, allowing for the determination of model parameters and the construction of site- and cycle-specific SFCCs. Finally, a Monte Carlo approach was applied to propagate measurement and parameter uncertainties, enabling the quantification of soil freezing and the classification of soil states for each site and cycle (Sect. 2.4). This framework facilitated continuous monitoring of soil freeze-thaw dynamics.

## 2.1 Data Collection

### 2.1.1 In Situ Soil Measurements

This study leverages in situ measurements of  $\varepsilon_{\text{eff}}$  and soil temperature to investigate and monitor the soil freezing and thawing processes and monitor the soil state processes. Our research spans eight networks located in diverse environments-ecozones (Table 1 and Fig. 2), including eastern boreal forests (Montmorency Forest (FM), La Romaine (LR), James Bay (Chapleau), western boreal forest (Candle Lake), prairies (Kenaston), and tundra ((BJ), Chapleau (CP) in eastern boreal forests, Candle Lake (BT) in western boreal forest, Kenaston (KN) in prairies, and Trail Valley Creek (George River (TV) and George River (GR) in tundra. Three types of soil moisture sensors—HydraProbe (Stevens Water), TEROS-12 (TEROS12 (METER Group), and CS616 (Campbell Scientific)—were deployed based on availability across the monitoring networks. HydraProbe and TEROS-12-TEROS12 simultaneously measure soil temperature and moisture, whereas the CS616 requires a separate soil temperature sensor (CS109SS-L) for temperature measurements. We provided an overview of these sensors, including their measurement principles and operational specifics, in Appendix A. At most sites, soil moisture probes were horizontally inserted to a depth of 5-5 cm, primarily within the organic layer unless it was notably thin, in which case measurements extended into the mineral layer. For the TEROS-12-TEROS12 and HydraProbe, insertion was horizontal at this depth. In the Chapleau network, the CS616, with its 30-30 cm needle, was inserted at a 20-degree-20° angle to integrate measurements over the top 10-10 cm of soil, with the midpoint depth set at 5-5 cm, thereby ensuring comparability with other sites (Fig. A1). Each site typically features a single sensor, except for Chapleau and Trail Valley Creek. Chapleau includes 24-24 CS616 sensors distributed across four 200 × 200-200 × 200 m plots, each representing a different forest type (Hanes et al., 2023). Since only one soil temperature sensor was available in the middle of each plot, data from multiple CS616 sensors were averaged to represent the soil conditions of that plot. At Trail Valley Creek, 12-12 HydraProbes were distributed across six sites (Montpetit et al., 2024, 2025), and data from each sensor were analyzed separately. Site- and sensor-specific calibration was not performed prior to installation; however, the use of manufacturer specifications and previously published validation studies provides confidence in the measurement accuracy of the deployed sensors within their expected uncertainty ranges (Seyfried and Murdock, 2004; Pardo Lara et al., 2021; Kelleners et al., 2005; Logsdon, 2009; Cominelli et al., 2024; Fragkos et al., 2024). A general quality control procedure was applied by removing physically implausible values, defined as soil temperatures outside the range of  $-60$  to  $60$  °C and permittivity values outside the range of 1-to-90-1 to 90. All in situ measurements were then subjected to a standardized preprocessing workflow. Data were resampled to a uniform hourly

**Table 1.** Summary of soil moisture sensor deployment across our networks

<del>Land-Cover</del> <u>Ecozone</u>	Network Name	Sensor Type <sup>†</sup>	Sensor Depth (cm)	Number of Sites (Probes)	Temporal Coverage
Eastern boreal forest	James Bay	TEROS 12	5	9 (9)	2020-08 to 2022-06
	Montmorency Forest	TEROS 12	5	10 (10)	2020-10 to 2024-06
	La Romaine	TEROS 12	5	3 (3)	2022-08 to 2023-07
	Chapleau	CS616	0–10 <sup>†</sup>	4 (24)	2017-08 to 2022-06
Western boreal forest	Candle Lake	HydraProbe	5	17 (17)	2022-08 to 2023-05
Prairies	Kenaston	HydraProbe	5	37 (37)	2014-08 to 2018-06
Tundra	Trail Valley Creek	HydraProbe	5	6 (12)	2018-09 to 2019-03
	George River	TEROS 12	5	1 (1)	2022-09 to 2023-07

<sup>†</sup> All sensors include built-in soil temperature measurement, except the CS616, which requires a separate soil temperature sensor (CS109SS-L).

<sup>†</sup> The CS616 is angled at 20°, measuring the top 10 cm of soil with a midpoint at 5 cm.

170 resolution, and a continuous time index was constructed to ensure temporal consistency. Missing values were filled using  
 linear interpolation; however, interpolated values were used solely for categorical soil state labeling and were excluded from  
 all curve-fitting analyses to preserve the integrity of model-derived parameters. The distribution of sites within each network  
 is strategically designed to capture the ecological diversity and maximize spatial variability, influenced by the challenging  
 terrain and limited accessibility of the network areas. ~~Our goal is to comprehensively represent the diversity of each network,~~  
 175 ~~thereby enhancing our understanding of regional soil dynamics.~~ Detailed characteristics for each site—including geographic  
 coordinates, soil textural composition (clay, sand, and silt percentages), organic content, specific soil types, elevation and  
 stratification of soil layers—are ~~are~~ available through an interactive map hosted in a GitHub repository (Soil-Temperature-  
 Permittivity-Monitoring-Sites) (Salmabadi et al., 2025).

### 2.1.2 Ancillary Data

180 Air temperature data were obtained from the ERA5-Land reanalysis developed by the European Centre for Medium-Range  
 Weather Forecasts (ECMWF; (C3S, 2018)). ERA5-Land provides hourly 2 m air temperature at 0.25° spatial resolution and  
 assimilates global observations within a physics-based numerical model to produce a consistent reanalysis extending from  
 1940 to the present. Snow cover data were derived from the Interactive Multisensor Snow and Ice Mapping System (IMS)  
 produced by the U.S. National Ice Center (U.S. National Ice Center, 2004), which provides daily binary snow-cover maps for  
 185 the Northern Hemisphere at 4 km resolution since 2004. The IMS product integrates multisensor satellite imagery and in situ  
 observations. For each study site, snow-cover and air-temperature values were extracted from the corresponding IMS and  
 ERA5-Land grid cells.



**Figure 2.** Geographic distribution of monitoring networks across Canadian landscapes. The land cover map is adapted from Latifovic (2019).

## 2.2 Data Preprocessing

The data preprocessing stage began by converting the raw outputs of the sensors into  $\varepsilon_{\text{eff}}$  for the bulk soil. This process varied depending on the sensor type, as each sensor produced different raw outputs. Detailed explanations of these sensor-specific preprocessing steps are provided in Appendix A. Next, we identified freezing and thawing cycles based on trends in soil temperature and  $\varepsilon_{\text{eff}}$ . A freezing cycle was defined as the period when soil temperature started decreasing and reached its minimum, while a thawing cycle extended from this minimum until temperatures rose above zero. This approach aimed to capture the main freezing and thawing events while excluding minor fluctuations, where temperatures briefly rose above or fell below zero within a narrow range, resulting in incomplete or transient freezing or thawing. Specifically, any fluctuations within  $\pm 2\sigma_T$  of  $0^\circ\text{C}$ , where  $\sigma_T$  represents the instrument-specific temperature uncertainty, were ignored (see Appendix A for details on sensor uncertainty). If, during a freezing cycle, the soil temperature never dropped below the  $-\sigma_T$  threshold and  $\varepsilon_{\text{eff}}$  remained relatively unchanged, we classified these sites as never frozen. Although curve fitting was not feasible for these [sites-cycles](#) due to insufficient data in Zones 2 and 3, they were retained for [further analysis to investigate the freezing process across our monitoring networks. In this analysis, we](#) [subsequent analysis of freeze monitoring across our networks.](#) [We](#) assumed that the total water content in the system remained equal to the initial water content and did not change during the freezing or thawing processes (He and Dyck, 2013). We monitored  $\varepsilon_{\text{eff}}$  throughout both freezing and thawing cycles to

validate this assumption. We interpreted significant, sudden surges in  $\varepsilon_{\text{eff}}$  as indicators of additional water entering the system, violating this assumption. Consequently, we excluded such cycles from further analysis. While this assumption generally held during freezing cycles, it was often invalid during thawing cycles, primarily due to snowmelt introducing substantial amounts of water into the soil. As a result, the SFCC could be reliably constructed for freezing cycles, but constructing the STCC from in situ measurements during thawing cycles was often not feasible. ~~Since this study aimed to use site- and cycle-specific SFCC/STCC to determine the degree of soil freezing and classify soil states, we applied the SFCC from each freezing cycle to the subsequent thawing cycle at the same site. Although differences between SFCC and STCC—primarily driven by hysteresis effects—are pronounced in laboratory settings, previous studies (Pardo Lara et al., 2020; Mavrovic et al., 2020) found no visually discernible differences in situ. We assumed that the SFCC could reliably represent the STCC until a significant change in total soil water content, marked by a sudden surge in  $\varepsilon_{\text{eff}}$ , which approximately corresponds to the snowmelt event. To assess the reliability of applying the SFCC for thawing cycles, we evaluated its performance over the full thawing cycle and up to the snowmelt date. Therefore, in this study we focused exclusively on freezing cycles, excluding thawing cycles from further analysis.~~

The final step in the preprocessing of in situ data involved ensuring a balanced dataset to prevent overfitting during the curve-fitting process. In practice, the distribution of data across temperature ranges was often uneven, which could bias the fitting process. We averaged  $\varepsilon_{\text{eff}}$  values within a  $0.1^\circ\text{C}$  temperature range to address this imbalance, corresponding to the sensors' temperature resolution. This approach not only compensated for the uneven distribution but also reduced noise caused by diurnal temperature fluctuations. Such fluctuations, while absent in controlled laboratory settings, were common in in situ environments.

## 2.3 Data Processing

### 2.3.1 SFCC Model

In this study, we applied the theoretical model introduced by ~~Bai et al. (2018)~~ [Bai et al.](#) to construct the SFCC, which estimates liquid water content as a function of soil temperature:

$$\theta_{lw} = \begin{cases} (\theta_{\text{int}} - \theta_{\text{res}})e^{b(T_{\text{soil}} - T_f)} + \theta_{\text{res}} & \text{if } T_{\text{soil}} < T_f \\ \theta_{\text{int}} & \text{if } T_{\text{soil}} \geq T_f \end{cases} \quad (1)$$

where  $\theta_{lw}$ ,  $\theta_{\text{int}}$ , and  $\theta_{\text{res}}$  represent the liquid, total (initial water content prior to freezing), and residual water content, respectively.  $T_{\text{soil}}$  is the soil temperature,  $T_f$  is the freezing ~~point~~ [onset temperature](#), and  $b$  controls the ~~steepness of the transition curve~~ [transition sharpness](#), representing the shape factor of the distribution function ( $^\circ\text{C}^{-1}$ ).

The relationship between the  $\varepsilon_{\text{eff}}$  and  $\theta_{lw}$  can be physically derived using mixing models (Amankwah et al., 2022; Kelleners and Norton, 2012; Roth et al., 1990), which express effective (bulk) permittivity as a volume-weighted average of soil components:

$$\varepsilon_{\text{eff}}^{\alpha} = \theta_{lw} \varepsilon_{lw}^{\alpha} + \theta_{\text{ice}} \varepsilon_{\text{ice}}^{\alpha} + (n - \theta_{lw} - \theta_{\text{ice}}) \varepsilon_{\text{air}}^{\alpha} + (1 - n) \varepsilon_{\text{soil}}^{\alpha} \quad (2)$$

where  $n$  represents the soil porosity, and  $\varepsilon_{\text{eff}}$ ,  $\varepsilon_{\text{soil}}$ ,  $\varepsilon_{lw}$ ,  $\varepsilon_{\text{ice}}$ , and  $\varepsilon_{\text{air}}$  are the relative dielectric permittivities (dimensionless) of bulk soil, soil solids, liquid water, ice, and air, respectively. The parameter  $\alpha$  depends on soil structure and composition, ranging from -1 (parallel arrangement) to 1 (series arrangement), with  $\alpha \neq 0$  (Amankwah et al., 2022). Solving for  $\theta_{lw}$  gives:

$$\theta_{lw} = \frac{\varepsilon_{\text{eff}}^{\alpha} - (1 - n) \varepsilon_{\text{soil}}^{\alpha} - n \varepsilon_{\text{air}}^{\alpha} - \theta_{\text{ice}} (\varepsilon_{\text{ice}}^{\alpha} - \varepsilon_{\text{air}}^{\alpha})}{\varepsilon_{lw}^{\alpha} - \varepsilon_{\text{air}}^{\alpha}} \quad (3)$$

This equation defines the relationship between  $\theta_{lw}$  and  $\varepsilon_{\text{eff}}$ , where  $\varepsilon_{\text{air}}$ ,  $\varepsilon_{lw}$ , and  $\varepsilon_{\text{ice}}$  are known constants with minimal temperature dependence, while  $n$ ,  $\alpha$ , and  $\varepsilon_{\text{soil}}$  vary with soil composition and structure and are treated as unknowns. We modified the model by Bai et al. (2018) (Eq. 1) by incorporating Eq. (3) to implement the SFCC in permittivity-temperature space. The detailed solution process is presented in Appendix B. The modified equation is:

$$\varepsilon_{\text{eff}}(T) = \begin{cases} ((\varepsilon_{\text{int}}^{\alpha} - \varepsilon_{\text{res}}^{\alpha}) e^{b(T_{\text{soil}} - T_f)} + \varepsilon_{\text{res}}^{\alpha})^{\frac{1}{\alpha}} & \text{if } T < T_f \\ \varepsilon_{\text{int}} & \text{if } T \geq T_f \end{cases} \quad (4)$$

Here,  $\varepsilon_{\text{int}}$  represents the pre-freezing  $\varepsilon_{\text{eff}}$ , corresponding to the system's total water content, which is assumed to approximate the initial water content (He and Dyck, 2013).  ~~$\varepsilon_{\text{res}}$  is the  $\varepsilon_{\text{eff}}$~~   $\varepsilon_{\text{res}}$  is the  $\varepsilon_{\text{eff}}$  associated with the residual water content. The parameter  $\alpha$ , as mentioned earlier, is an exponent that depends on the soil structure and composition. ~~To fully define the SFCC, it is necessary to estimate  $T_{\text{res}}$ , which marks the onset of Zone 3 in the SFCC (Fig.1). From Eq. (4), we have:~~

$$\varepsilon_{\text{eff}}(T)^{\alpha} = (\varepsilon_{\text{int}}^{\alpha} - \varepsilon_{\text{res}}^{\alpha}) e^{b(T - T_f)} + \varepsilon_{\text{res}}^{\alpha}$$

~~As  $T \rightarrow -\infty$ ,  $\varepsilon_{\text{eff}}(T)$  approaches  $\varepsilon_{\text{res}}$ . To determine the temperature at which  $\varepsilon_{\text{eff}}(T)$  approaches  $\varepsilon_{\text{res}}$ , we introduce a small threshold  $\delta$ :~~

$$(\varepsilon_{\text{int}}^{\alpha} - \varepsilon_{\text{res}}^{\alpha}) e^{b(T - T_f)} < \delta$$

250 ~~Solving for  $T$ :~~

$$T < \frac{\ln\left(\frac{\delta}{\varepsilon_{\text{int}}^{\alpha} - \varepsilon_{\text{res}}^{\alpha}}\right)}{b} + T_f$$

~~Thus, the temperature  $T_{\text{res}}$ , where  $\varepsilon_{\text{eff}}(T)$  reaches the plateau, is approximately:~~

$$T_{\text{res}} \approx \frac{\ln\left(\frac{\delta}{\epsilon_{\text{int}}^\alpha - \epsilon_{\text{res}}^\alpha}\right)}{b} + T_f$$

255 In our calculations, we used  $\delta = 0.01$ , which allows us to determine the temperature where the difference between  $\epsilon_{\text{eff}}(T)$  and  $\epsilon_{\text{res}}$  is negligible.

In summary, In short, by incorporating a dielectric mixing model into the theoretical framework proposed by Bai et al. (2018) (Eq. 1), we constructed Bai et al.'s model, we formulated the SFCC in the permittivity–temperature space. The resulting SFCC model (Eq. 4) calculates  $\epsilon_{\text{eff}}$ , where  $\epsilon_{\text{eff}}$  is expressed as a function of soil temperature  $T$ , using key parameters such as the shape factor of the distribution function  $b$  ( $1/^\circ\text{C}$ ), freezing point depression ( $T_f$ ), and the initial ( $\epsilon_{\text{int}}$ ) and residual ( $\epsilon_{\text{res}}$ ) permittivity, which are determined using optimization and curve-fitting techniques. Finally, calculating  $T_{\text{res}}$  (Eq. ??) identifies the temperature at which the soil is completely frozen, defining the onset of Zone 3 in the SFCC and completing its characterization through parameters  $b$  ( $1/^\circ\text{C}$ ),  $T_f$ ,  $\epsilon_{\text{int}}$ , and  $\epsilon_{\text{res}}$ , derived via curve fitting.

### 2.3.2 **Parameter Estimation for the SFCC Model** Fitting and Parameter Estimation

To derive the model parameters— $\epsilon_{\text{int}}$ ,  $\epsilon_{\text{res}}$ ,  $b$ , and  $T_f$ —and construct the SFCC, we applied a systematic data processing and curve-fitting approach tailored to our SFCC model (Eq. 4). ~~To ensure accuracy and physical plausibility, we~~ We used non-linear least squares optimization with initial guesses and parameter bounds. The curve fitting was conducted using the `curve_fit` function from the SciPy library (version 1.13.1) in Python (Virtanen et al., 2020), employing the Trust Region Reflective (TRF) algorithm, which optimizes parameter values while keeping them within predefined bounds. ~~We fitted the SFCC model (Eq. 4) to each individual freezing cycle, generating site- and cycle-specific SFCCs to estimate the degree of soil freezing.~~ Since the fitting is performed independently for each site and cycle, variations in absolute  $\epsilon_{\text{eff}}$  values, caused by differences in probe operating frequencies—due to the frequency-dependent dielectric properties of water and bulk soil—do not affect soil state monitoring.

To ensure that the data used for model fitting primarily reflect the freezing process, we included only measurements where  $T_{\text{soil}} \leq 2^\circ\text{C}$ , capturing temperatures where freezing processes are actively occurring. During initial analyses,  $\alpha$ , the exponent representing soil structure in the dielectric mixing model (Eq. 3), consistently converged to boundary values without improving model fit, indicating low sensitivity. This issue likely stems from eliminating parameter  $B$  when deriving the SFCC model from Bai et al. (2018)'s framework (Eq. B17). This reduction decreases the model's dependence on soil parameters such as porosity and soil solid permittivity, both of which influence  $\alpha$ . To enhance model stability and interpretability, we fixed  $\alpha$  at 0.505, a commonly used value (Pardo Lara et al., 2020; Seyfried et al., 2005). We set the lower bound of  $\epsilon_{\text{res}}$  at 1, the lowest measurable probe range, and constrained the upper bound to remain below  $\epsilon_{\text{int}}$  to prevent unrealistic values. The initial effective permittivity,  $\epsilon_{\text{int}}$ , representing pre-freezing soil permittivity, was initialized as the mean  $\epsilon_{\text{eff}}$  within  $\sigma_T^\circ\text{C} \leq T_{\text{soil}} \leq 2^\circ\text{C}$ , where  $\sigma_T$  represents the instrument-specific temperature uncertainty (see Appendix A for details on sensor uncertainty). This range ensures that mainly unfrozen-state data (Zone 1) contribute to the estimate, accounting for sensor uncertainty. The bounds

for  $\varepsilon_{\text{int}}$  were set as the observed minimum and maximum  $\varepsilon_{\text{eff}}$  within this range. The exponential constant  $b$ , which controls  
 285 the transition from  $\varepsilon_{\text{int}}$  to  $\varepsilon_{\text{res}}$ , was initialized at 1.01, 0, with a lower bound of 0.1, 0.1 to prevent overly gradual transitions  
 and no upper bound. For the ~~freezing temperature~~  $T_f$ , we allowed values up to  $+1^\circ\text{C}$  to accommodate known measurement  
 biases and sensor discrepancies. For instance, ~~Pardo Lara et al. (2020)~~ Pardo Lara et al. (2020, 2021) suggested that dielectric  
 sensors may detect permittivity changes indicative of freezing before thermistors register subzero temperatures, likely due to  
 differences in placement, thermal inertia, or measurement volume (~~Pardo Lara et al., 2021~~). These discrepancies can cause  $T_f$   
 290 to register as slightly positive, ~~particularly during rapid temperature transitions~~.

To assess the robustness and uncertainty of ~~our~~ fitted parameters  $(\varepsilon_{\text{int}}, \varepsilon_{\text{res}}, b, T_f)$ , we applied bootstrapping, resampling in  
 situ soil temperature and  $\varepsilon_{\text{eff}}$  data 1,000-1,000 times. To ensure representative selection across temperature ranges, we divided  
 the data into blocks and resampled within each block with replacement. This approach preserved the natural distribution of  
 $\varepsilon_{\text{eff}}$  across the soil temperature range while introducing variability across iterations. ~~Each iteration generated a new dataset for~~  
 295 ~~curve fitting, enabling us to quantify parameter variability, construct confidence intervals, and identify potential biases.~~ The  
 resulting bootstrapped parameter distributions were used to compute mean values and standard deviations.

~~Although the SFCC could be constructed directly using the parameters from Sect. 2.3.2, accounting for measurement~~  
~~and model uncertainties was essential. To do so, Subsequently,~~ a Monte Carlo framework with  $N = 15,000$  simulations  
 was employed for each measurement point (i.e., each hourly soil temperature observation). Soil temperature ~~measurements~~  
 300 ~~were modeled as normally distributed~~ was modeled as a normal distribution,  $T_{\text{sim}} \sim \mathcal{N}(T_{\text{obs}}, \sigma_T^2)$ , with sensor-specific standard  
 deviations. ~~We quantified parameter uncertainties using bootstrap statistics. Each variable~~ Each parameter ( $M$ )—where  $M \in \{T_f, T_{\text{res}}, \varepsilon_{\text{int}}, \varepsilon_{\text{res}}, b\}$ —  
~~independently~~ independently sampled from a normal distribution,  $\mathcal{N}(\mu_M, \sigma_M^2)$  ~~with, where~~  $\mu_M$  and  $\sigma_M$  ~~, obtained from~~ were derived from  
~~the~~ the bootstrap analysis. ~~We discarded simulations that violated~~ Simulations violating physical constraints (i.e.,  $\varepsilon_{\text{int}} < \varepsilon_{\text{res}}$  ~~or~~  
 $T_{\text{res}} > T_f$ ) ~~to ensure result~~ were discarded to maintain physical validity. For each ~~simulation, an effective permittivity,~~  
 305  ~~$\varepsilon_{\text{modeled}}$ , was computed and normalized ( $\varepsilon_{\text{normalized}} = \frac{\varepsilon_{\text{modeled}} - \varepsilon_{\text{res}}}{\varepsilon_{\text{int}} - \varepsilon_{\text{res}}}$ ) yielding values between 0 (fully frozen) and 1 (fully unfrozen).~~  
~~The degree of soil being unfrozen was determined as the mean of  $\varepsilon_{\text{normalized}}$  across all  $N = 15,000$  simulations, given by~~  
 $\frac{1}{N} \sum_{i=1}^N \varepsilon_{\text{normalized}, i}$ . ~~Consequently, the degree of soil freezing, which can be interpreted as the probability of frozen ground,~~  
~~was expressed as  $1 - \frac{1}{N} \sum_{i=1}^N \varepsilon_{\text{normalized}, i}$ .~~ Because satellite overpasses motivate a daily product, we aggregated the hourly  
 probabilities to daily means. Daily soil state was then labelled as frozen if the mean freeze probability exceeded 0.9, unfrozen  
 310 if it was below 0.1, and in transition (partially frozen) otherwise. These thresholds were selected to ensure high confidence  
 in identifying predominantly frozen or unfrozen conditions, while intermediate values captured transitional states associated  
~~with partial freezing.~~ valid simulation, the modeled effective permittivity  $\varepsilon_{\text{fitted}, i}$  was computed for each realization, and the  
~~ensemble mean was used as the expected effective permittivity,  $\bar{\varepsilon}_{\text{fitted}} = \frac{1}{N} \sum_{i=1}^N \varepsilon_{\text{fitted}, i}$ .~~

Following parameter estimation, a multi-step filtering process was applied to ensure the physical validity and reliability of  
 315 the fitted SFCCs. Only cycles occurring during fall and winter (1 September–1 March), hereafter referred to as the freezing  
season, were retained, while short transient events observed in spring were excluded. The filtering process removed cycles  
with  $R^2 < 0.6$ , visually detected anomalies (e.g. irregular water content changes during freezing), and unreliable parameter  
estimates (boundary values for  $T_f$  or  $b$ , or excessively wide confidence intervals). Extreme outliers in  $T_f$  and  $b$  were also

320 excluded by retaining only the central 95% of the distribution (2.5th–97.5th percentiles). We applied Bayesian hierarchical  
partial pooling in *PyMC* to obtain stabilized estimates of  $b$  and  $T_f$  across sites and networks within ecozones. This hierarchical  
structure allowed information sharing among data-sparse sites and networks, reducing uncertainty while preserving genuine  
spatial differences. For  $b$ , we modeled  $\log b$  with network- and site-level random intercepts in a non-centered parameterization,  
using a Student- $t$  likelihood with heteroskedastic scales equal to the bootstrap standard error (SE) of  $\log b$  combined with a  
residual term. For  $T_f$ , we used an analogous hierarchy on the original C scale, with observation-level SEs and an additional  
325 residual variance. Weakly informative Normal priors were assigned to means, and Half-Student- $t$  priors to variance components.  
Models were fit using the No-U-Turn Sampler (NUTS), and convergence ( $\hat{R} \leq 1.01$ , high effective sample sizes) and numerical  
stability (no or rare divergences) were confirmed. Sampler energy diagnostics were adequate (E-BFMI  $\geq 0.50$ ), and out-of-sample  
performance was reliable (PSIS-LOO with 100% of points  $\hat{k} \leq 0.7$ ).

## 2.4 Data Postprocessing

### 330 2.4.1 Probability of Frozen Ground

#### 2.3.2 SFCC-based Soil State Classification

The probability of frozen ground ( $P_{\text{frozen}}$ ; hereafter referred to as the freezing probability), which can also be interpreted as  
degree of soil freezing at the network level, was computed by propagating uncertainty from the hierarchical posterior  
distributions of  $T_f$  and  $b$ . For each network, paired posterior samples  $\{(T_f^{(s)}, b^{(s)})\}_{s=1}^S$  were drawn from the *PyMC* hierarchical  
335 models, where  $b^{(s)} = \exp(b_j^{(s)})$  restores the parameter to its original scale. Soil temperature observations were perturbed  
according to sensor uncertainty,  $T_{\text{sim}}^{(s)} \sim \mathcal{N}(T_{\text{obs}}, \sigma_T^2)$ , where  $\sigma_T$  was assigned based on the sensor type. For each posterior  
draw, the freezing probability was evaluated using the normalized SFCC, and the results were averaged across all Monte Carlo  
samples to obtain the mean freezing probability at each timestamp.

#### 2.3.2 Temperature-based Soil State Classification

340 The conventional hard  $0^\circ\text{C}$  threshold was modified by introducing a probabilistic analogue that accounted for sensor uncertainty.  
Each hourly soil temperature observation was sampled 1000 times from a normal distribution,  $T_{\text{sim}} \sim \mathcal{N}(T_{\text{obs}}, \sigma_T^2)$ , where  $\sigma_T$   
represented the sensor-specific standard deviation. These samples were then passed through a logistic function,  $P_{\text{frozen}}(T) = \frac{1}{1 + \exp[s(T - T_0)]}$   
with  $T_0 = 0^\circ\text{C}$  and a steepness parameter  $s = 5$ , to compute a smoothed freeze probability. Daily mean probabilities were  
subsequently used to classify the soil as frozen if  $P_{\text{frozen}} > 0.5$ , and unfrozen otherwise. Because this temperature-based  
345 method could not resolve a transitional state, a neutral threshold of 0.5 was applied, and transitional days were therefore not  
explicitly represented in this scheme.

### 3 Results

#### 3.1 Model Parameter Analysis

##### 3.1 Evaluation of SFCC Fits and Parameter Analysis

350 A total of 204 freezing cycles were identified across all sites, and the SFCC model (Eq. 4) was fitted to each cycle separately. Since a mean  $R^2$  below 0.95 indicates a poor fit, cycles with an  $R^2$  value below 0.6 were excluded (4 cycles) for quality control. Additionally, 11 cycles were excluded due to unreliable parameter estimates as evidenced by frequent boundary values for  $T_f$ ,  $T_{res}$ , and  $b$  during bootstrapping. To further ensure robustness, we applied an interquartile range (IQR)-based filter to exclude cycles with excessively wide confidence intervals, defined as greater than  $Q3 + 3 \times IQR$  for each parameter separately, resulting in the removal of 35 cycles. A final visual inspection led to the exclusion of 8 additional cycles identified with anomalies, such as irregular water content changes during freezing. Following this rigorous filtering process, 146 freezing cycles were retained: 12 from tundra sites, 19 from boreal forest sites (8 from eastern boreal networks and 11 from western boreal networks), and 115 from prairie sites.

360 A total of 96 freezing cycles across all networks passed the filtering criteria and were retained for analysis. The performance of the SFCC curve-fitting process were evaluated by comparing fitted permittivity values  $\epsilon_{\text{eff,fit}}$  with in situ  $\epsilon_{\text{eff,Actual}}$  measurements of  $\epsilon_{\text{eff,observed}}$  (Fig. 3). Model performance We evaluated the reliability of the constructed SFCC in estimating the degree of soil freezing and classifying soil states by comparing SFCC-based predictions of  $\epsilon_{\text{eff,Predicted}}$ —obtained via Monte Carlo simulations—Goodness of fit was quantified using the coefficient of determination ( $R^2$ ), root mean square error (RMSE), and mean absolute error (MAE). Additionally, relative RMSE and MAE were calculated as percentages of the mean  $\epsilon_{\text{eff,Actual}}$  (normalized by the per-network dynamic range ( $\epsilon_{\text{eff,max}} - \epsilon_{\text{eff,min}}$ ; Table 2). Overall, the model demonstrated strong performance in predicting  $\epsilon_{\text{eff}}$ . However, high relative errors—SFCC model reproduced the observed permittivity well, achieving a mean  $R^2$  of 0.95 and relative RMSE and MAE of 5% and 3%, respectively. The best performance was observed in the BT and KN networks ( $R^2 > 0.9$ ; relative RMSE  $< 5\%$ ), whereas slightly lower fits ( $R^2 \approx 0.67$ ) were observed in tundra regions, likely due to multiple incomplete freezing and thawing cycles preceding the main freezing cycle. These fluctuations introduce uncertainties in the transitional zone, making it more challenging for the model to precisely predict  $\epsilon_{\text{eff}}$  FM and GR networks, likely reflecting sparse sampling of the transitional zone as freezing progressed rapidly.

370 The mean values, standard deviations across cycles ( $\sigma$ ), and mean bootstrapped standard deviations ( $\overline{\sigma_{\text{bootstrap}}}$ ) for each parameter were calculated to assess the freezing characteristics of soils in our networks across different landscapes. It is important to note that these networks may not be fully representative of the entire landcover but rather indicate strong spatial variability in freezing processes. The results of this section are summarized in Table ???. In the eastern boreal forest, the mean  $b$  was 3.41 ( $\sigma = 0.98$ ,  $\overline{\sigma_{\text{bootstrap}}} = 1.08$ ), the highest among all networks, suggesting a sharp freezing transition. In contrast, the western boreal forest had the lowest mean  $b$  at 1.33 ( $\sigma = 0.87$ ,  $\overline{\sigma_{\text{bootstrap}}} = 0.21$ ), indicating a more gradual freezing transition. The lowest  $T_{res}$  was observed in the prairies at  $-4.72^\circ\text{C}$  ( $\sigma = 3.18^\circ\text{C}$ ,  $\overline{\sigma_{\text{bootstrap}}} = 0.48^\circ\text{C}$ ), suggesting that prairie soils reach a completely frozen state at lower temperatures than other landcovers. In contrast, the eastern boreal forest exhibited

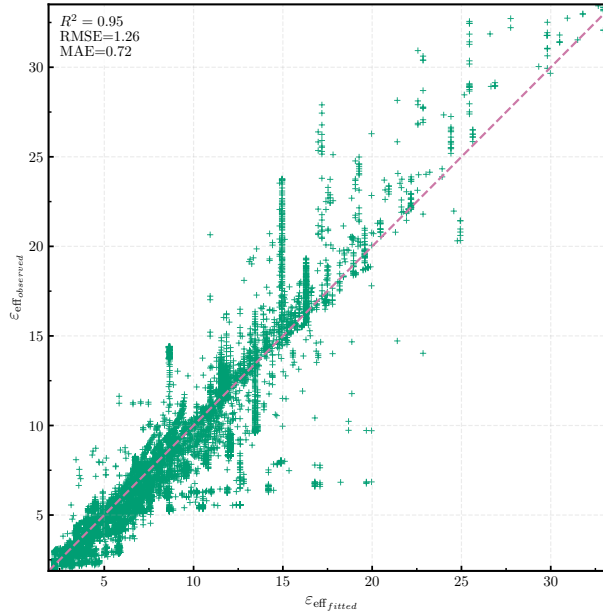


**Figure 3.** Comparison of in-situ (actual)  $\varepsilon_{\text{eff,observed}}$  and SFCC-predicted  $\varepsilon_{\text{eff,fitted}}$  for freezing cycles, color-coded by land-cover type.

380 a  $T_{\text{res}}$  of  $-1.07^{\circ}\text{C}$ , indicating that soils in this region freeze fully at relatively higher temperatures. The highest freezing-onset temperature ( $T_f$ ) was recorded in the eastern boreal forest at  $0.47^{\circ}\text{C}$  ( $\sigma = 0.20^{\circ}\text{C}$ ,  $\overline{\sigma_{\text{bootstrap}}} = 0.07^{\circ}\text{C}$ ), suggesting that soils in this region begin freezing at a higher temperature. Conversely, the western boreal forest exhibited a more depressed freezing temperature.

Summary of SFCC model parameters by land-cover

Land-cover	n	Mean $b$ ( $\sigma$ )	Mean $T_f$ ( $\sigma$ )	Mean $T_{\text{res}}$ ( $\sigma$ )
Eastern boreal forest	8	3.41 (0.98)	$0.47^{\circ}\text{C}$ (0.20 $^{\circ}\text{C}$ )	$-1.07^{\circ}\text{C}$ (0.43 $^{\circ}\text{C}$ )
Western boreal forest	11	1.33 (0.87)	$0.00^{\circ}\text{C}$ (0.67 $^{\circ}\text{C}$ )	$-3.32^{\circ}\text{C}$ (1.77 $^{\circ}\text{C}$ )
Prairie	115	1.63 (1.53)	$0.08^{\circ}\text{C}$ (0.27 $^{\circ}\text{C}$ )	$-4.72^{\circ}\text{C}$ (3.18 $^{\circ}\text{C}$ )
Tundra	12	2.6 (1.56)	$0.13^{\circ}\text{C}$ (0.23 $^{\circ}\text{C}$ )	$-2.45^{\circ}\text{C}$ (1.56 $^{\circ}\text{C}$ )

385

To further investigate the model parameters, we analyzed the distribution of  $b$ ,  $T_f$ , and  $T_{\text{res}}$  values (Fig. ??). The analysis reveals that extreme cases in the boxplots are rare, as expected, and cannot be classified as outliers due to the rigorous filtering applied to the cycles. The extreme  $b$  values observed in the prairie region are primarily associated with cycles recorded during spring. During this period, abundant water from snowmelt, combined with the absence of snow cover, allows diurnal air temperature fluctuations to drive rapid freezing cycles, resulting in elevated  $b$  values. For instance, the two cycles with  $b$  values greater than 6 correspond to  $\varepsilon_{\text{int}}$  values of approximately 36, significantly higher than the network average of 16.5. In the prairie region, the combination of high clay content and low moisture content prior to freezing generally leads to higher  $T_{\text{res}}$  values. Notably, the site with the lowest recorded  $T_{\text{res}}$  (UG17,  $-14.94^{\circ}\text{C}$ ) also exhibited the highest clay content (41.1%; (Tetlock et al., 2019)) among all sites. In the western boreal forest, one extreme  $T_f$  value ( $-1.63^{\circ}\text{C}$ ) was observed at a site within the Candle Lake network, where the moisture content was exceptionally low. The  $\varepsilon_{\text{int}}$  for this site was approximately 3.57, the lowest among the boreal forest sites, which contributed to the pronounced depression in  $T_f$

390

395

**Table 2. Model performance metrics for predicting  $\epsilon_{\text{eff}}$  across different land cover types during freezing periods.** Performance of SFCC curve fitting by network. Relative errors are RMSE and MAE (shown in parentheses as percentages of  $\epsilon_{\text{eff,Actual}}$ ) were normalized by the mean  $\epsilon_{\text{eff,Actual}}$  per-network dynamic range. “Overall (balanced)” represents random subsampling with an equal number of samples per network to mitigate overrepresentation effects.

Land-Cover-Type/Network	$R^2$	RMSE	MAE
Eastern-boreal-forest-BJ	0.85 (0.93)	1.25 (18.28) 1.20 (7.2%)	0.81 (11.85) 0.94 (5.7%)
Western-boreal-forest-BT	0.94 (0.95)	0.29 (8.03) 3.7%	0.18 (4.99) 2.3%
Prairies-CP	0.82	0.80 (8.6%)	0.61 (6.6%)
FM	0.66	2.34 (11.7%)	1.70 (8.5%)
GR	0.67	2.13 (8.4%)	1.17 (4.6%)
KN	0.95	1.07 (10.94) 1.14 (3.8%)	0.65 (6.65) 0.71 (2.4%)
Tundra-LR	0.87	0.43 (7.4%)	0.25 (4.2%)
TV	0.86	1.71 (39.20) 2.07 (6.5%)	0.87 (19.94) 1.19 (3.8%)
Overall	0.95	1.16 (14.58) 1.26 (4.0%)	0.64 (8.05) 0.72 (2.3%)
Overall (balanced)	0.89	1.54 (4.9%)	0.86 (2.7%)

Box plots showing the distribution of model parameters: shape factor  $b$  (a),  $T_{\text{res}}$  (b), and  $T_f$  (c) across different land cover types.

400 Figure 4 presents the cumulative distribution functions (CDFs) of the residuals, highlighting key patterns in the model's performance across different land cover types. SFCC curve-fitting performance across networks and illustrating the distribution of residuals-residual distributions as a function of soil temperature. Across all regions/networks, residuals are smallest at temperatures well below freezing below  $T_f$ , demonstrating the model's strong ability to predict soil effective permittivity accurately-strong ability of the SFCC fitting to reproduce  $\epsilon_{\text{eff}}$  under stable frozen conditions where variability in total water content is minimal. Conversely, residuals increase significantly near the freezing point, where abrupt changes in soil temperature and water content introduce greater variability, challenging the model's predictive accuracy. At temperatures above freezing, Residuals increase near  $T_f$ , where sparse data in the transitional zone limits the robustness of the curve fitting. Above  $T_f$ , residuals remain larger compared to higher than subfreezing conditions, likely due to increased fluctuations in total reflecting fluctuations in water content caused by rainfall events, as expected, transpiration, or drainage. The CDFs exhibit steep slopes near zero across all land cover types/networks, indicating minimal systematic bias in the model and confirming that the majority of most residuals are small, thereby supporting the model's overall robustness-supporting the overall robustness of fitting process. However, the eastern boreal forest, prairie, and tundra regions exhibit pronounced tails in their residual distributions, indicating instances of underprediction and overprediction. In contrast, the western boreal forest demonstrates the most accurate predictions, as evidenced by its steep CDF near zero and minimal tail lengths. This superior performance may be attributed to the region's drier conditions and smaller fluctuations in total water content, which enhance model reliability are evident in the tails of distributions, corresponding to rapid freezing cycles that the SFCC cannot fully capture.

405

410

415

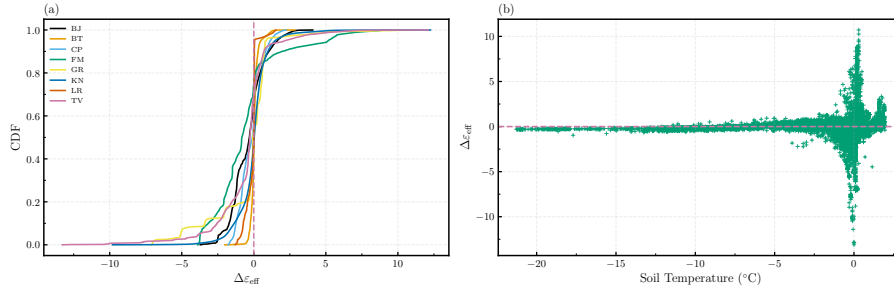


**Figure 4.** CDFs of residuals across ~~landcover types networks~~ (a), showing that most residuals are small, with steep slopes near zero, indicating minimal ~~systematic~~-bias. Residuals as a function of soil temperature (b), with ~~random subsampling of~~ an equal number of ~~data points randomly selected samples~~ per ~~landcover to ensure fair network for balanced~~ representation.

### 3.2 Model Performance

We also tested the model's performance during thawing cycles, both for the full thawing period and before snowmelt (or any water infiltration into the soil), to evaluate our assumption that the SFCC is equivalent to the STCC. The model performed well in estimating  $\epsilon_{\text{eff}}$  before snowmelt. Across land cover types, the coefficient of determination ( $R^2$ ) values were 0.54 for the eastern boreal forest sites, 0.70 for the western boreal forest sites, and 0.65 for the prairie sites. RMSE values were 0.84

420 ~~Figure 5 shows the forest plots of  $T_f$  (panel a) and  $b$  (panel b) across monitoring networks. Black circles denote cycle-level estimates with 95% confidence intervals, while red squares represent network-level means. Networks are ordered by mean  $T_f$ , with sample sizes ( $N$ ) indicated. To integrate information across sites, networks, and ecozones and stabilize estimates in data-sparse regions, we applied Bayesian hierarchical (partial-pooling) models for both parameters. Table 3 reports posterior means and 95% credible intervals for  $b$  and  $T_f$  under hierarchical partial pooling. Across all  $N = 96$  freezing cycles,  $b$  values ranged from 0.14 to 5.25, with most cycle-level estimates falling between 0.6 and  $2.1\text{ }^\circ\text{C}^{-1}$ . Network-level posterior means from the hierarchical model ranged from  $0.92$  to  $3.47\text{ }^\circ\text{C}^{-1}$ , revealing distinct differences in transition sharpness across networks. KN (prairie) and BT (western boreal) exhibited the lowest  $\hat{b}$  ( $< 1.5$ ), indicating gradual soil freezing transitions, while all other~~

430 ~~networks (BJ, CP, FM, LR, GR, TV) showed higher  $\hat{b}$  ( $> 3$ ), consistent with sharper phase-change behavior. Posterior credible intervals widened with increasing  $\hat{b}$ , reflecting higher uncertainty in steep, rapidly changing transitions (Fig. 5). Cycle-level  $T_f$  ranged from  $-0.54\text{ }^\circ\text{C}$  to  $0.85\text{ }^\circ\text{C}$ , with most estimates between  $-0.01\text{ }^\circ\text{C}$  and  $0.40\text{ }^\circ\text{C}$ . Network-level posterior means were slightly positive ( $0.15 - 0.44\text{ }^\circ\text{C}$ ). BJ, FM, LR, and CP exhibited the highest freezing points ( $\hat{T}_f \approx 0.40\text{ }^\circ\text{C}$ ), whereas KN, GR, and TV showed the lowest ( $\hat{T}_f \approx 0.15\text{ }^\circ\text{C}$ ).~~

### 435 3.2 Model Application to Field Data

To illustrate the application of our SFCC model (Eq. 4) and its integration with in situ data, we ~~presented five~~ present four example sites from different ~~monitoring networks~~, each exhibiting distinct freezing behaviors: eastern boreal forest (networks and ecozones, each representing a distinct freezing regime: EC17 from KN (prairie; Fig. 8 and Fig. ??), 6), BT17 from BT

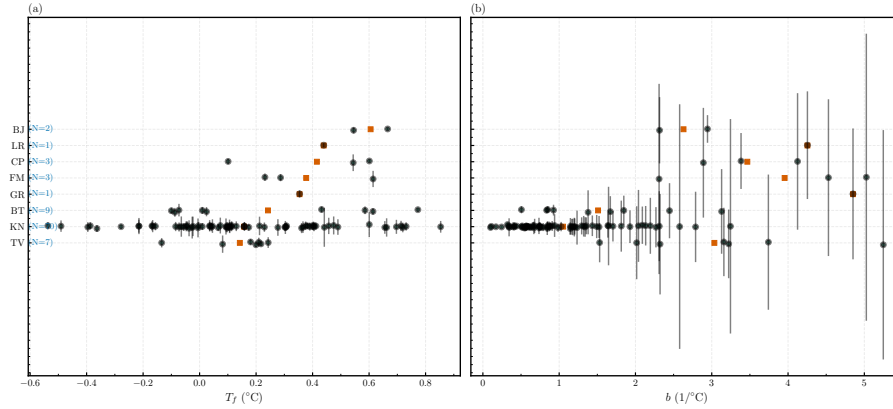


**Figure 5.** Forest plots showing the distribution of model parameters across networks: freezing point  $T_f$  (a) and shape factor  $b$  (b). Squares indicate network means, and circles represent individual freezing cycles with vertical bars showing 95% confidence intervals.

**Table 3.** Posterior means and 95% credible intervals of  $b$  and  $T_f$  from hierarchical partial pooling across networks.

Network	$\hat{b}$ (18.00%), 0.13 (4.43%), and 1.46 °C <sup>-1</sup>	$\hat{b}_{2.5\%}$ (19.65%), while MAE values were 0.44 °C <sup>-1</sup>	$\hat{b}_{97.5\%}$ (9.56%), 0.10 °C <sup>-1</sup>	$\hat{T}_f$
TV	2.99	1.77	4.32	
GR	3.14	1.40	5.18	
BT	1.42	0.90	1.99	
BJ	3.26	1.73	5.00	
FM	3.47	1.75	5.43	
LR	3.45	1.69	5.57	
CP	3.43	1.86	5.27	
KN	0.92	0.74	1.09	

(western boreal forest; Fig. 7), prairie (BJ01 from BJ (eastern boreal forest; Fig. 68), and tundra (GR01 from GR (tundra; Fig. 9). Each example consisted of includes two panels: the first panel (a) depicted shows the fitted SFCC overlaid on the processed in situ measurements of in situ soil temperature and permittivity, with vertical lines indicating  $T_f$  and  $T_{res}$ . The second panel  $\epsilon_{eff}$  measurements with  $T_f$  marked; panel (b) displayed the presents the corresponding time series of soil temperature for the same site, color-coded by the probability of frozen ground (degree of soil freezing). To further summarize the results, we included, freezing probability, ERA5 air temperature, and IMS snow cover. To summarize all networks, Fig. 10, which shows the monthly average of the probability of frozen ground over the entire data period for all sites within each network. This visualization provided insight into the average freezing and thawing patterns at each station and network. In the eastern boreal forest, soils rarely freeze completely during winter (Fig. 10), reflecting high water retention and the insulating effect of snow and vegetation cover. This leads to either prolonged transitional states displays the monthly mean freezing probability, with monthly mean air and soil temperatures overlaid on each tile. To compare networks quantitatively, soil states were classified

450 at hourly resolution as frozen if  $P_{\text{frozen}} > 0.75$ , unfrozen if  $P_{\text{frozen}} < 10^{-6}$ , and transitional (partially frozen) otherwise. Daily states were assigned by majority rule.

BJ, CP, FM, and LR—a phenomenon known as the zero curtain effect—located in the eastern boreal forest—~~or unfrozen soil throughout the year. On average, we recorded 23 frozen days and 46 transitional days in this region~~remained predominantly unfrozen or partially frozen throughout the freezing season, with no periods of complete freezing despite persistent snow cover (> 90% from December to February) and subzero air temperatures. Their soils stayed near 0°C, yielding moderate freezing probabilities ( $P_{\text{frozen}} < 0.65$ ). For instance, FM and CP remained partially frozen for approximately 125 days, while BJ and LR showed shorter transitional periods ( $\approx 100$  days) with  $\approx 75$  unfrozen days. In contrast, ~~the western boreal forest, characterized by drier conditions compared to its eastern counterpart, experiences more extensive freezing while still retaining some transitional states. On average, we recorded 73 frozen days and 76 transitional days at these sites. As expected, tundra sites exhibited the longest frozen periods, with an average of 145 frozen days due to consistently low temperatures, along with 52 transitional days. Prairie soils began freezing earlier than boreal forest soils, likely due to the absence or shallow depth of snow cover and the lack of vegetation, as these sites are primarily agricultural lands. This lack of insulation made prairie soils more susceptible to air temperature fluctuations (Fig 6), allowing soil temperatures to drop more rapidly~~BT (western boreal) exhibited extensive freezing from December onward (90 frozen and 30 transitional days), coinciding with subzero air temperatures and complete snow cover. Tundra networks (TV, GR) recorded the coldest soil and air temperatures from December to February (soil and air consistently below  $-2^{\circ}\text{C}$  and  $-10^{\circ}\text{C}$ , respectively) and persistent snow cover ( $\approx 100\%$ ), resulting in almost continuous frozen conditions ( $P_{\text{frozen}} > 0.95$ ) lasting 135 and 95 days for TV and GR respectively. The KN (prairie) network showed an intermediate response: although mean air temperatures ( $\approx -3^{\circ}\text{C}$ ) were comparable to eastern forest networks, soil cooling began earlier (November,  $T_{\text{soil}} \approx 0.9^{\circ}\text{C}$ ) and remained frozen through February ( $P_{\text{frozen}} > 0.9$ ) under shallow or intermittent snow (50 – 95%). On average, ~~we recorded 71 frozen days and 71 transitional days in the prairies. Additionally, prairie soils thaw earlier than other landcover types, reflecting their sensitivity to air temperature variations~~about 70 days were classified as frozen and 60 days as transitional at KN. Overall, while all networks experienced similar subzero air temperatures and persistent snow cover from December to February, only tundra (TV, GR), western boreal (BT), and prairie (KN) networks exhibited sustained frozen states, whereas eastern forest networks (BJ, CP, LR, FM) remained largely in transitional or unfrozen conditions.

### 3.3 SFCC-Based Soil Classification vs. Temperature-Based Classification

The agreement between the SFCC-based classification and the temperature-based method varied systematically across different land cover types (Fig. ??). In the eastern boreal forest, the overall agreement was 38.0%. Approximately 86% of the transitional days identified by the SFCC method were mislabeled as “unfrozen,” leading to a substantial overestimation of unfrozen conditions. In the western boreal forest, agreement was 54.1%; here, nearly 87% of transitional days were misclassified as “frozen,” resulting in an overestimation of frozen ground. The prairies showed 67.2% agreement, with a similar pattern—about 94% of transitional days were labeled as “frozen,” again inflating the estimated extent of frozen conditions. The tundra exhibited the highest agreement at 75.0%, likely due to a shorter transitional phase; in this region, around 64% of transitional days were

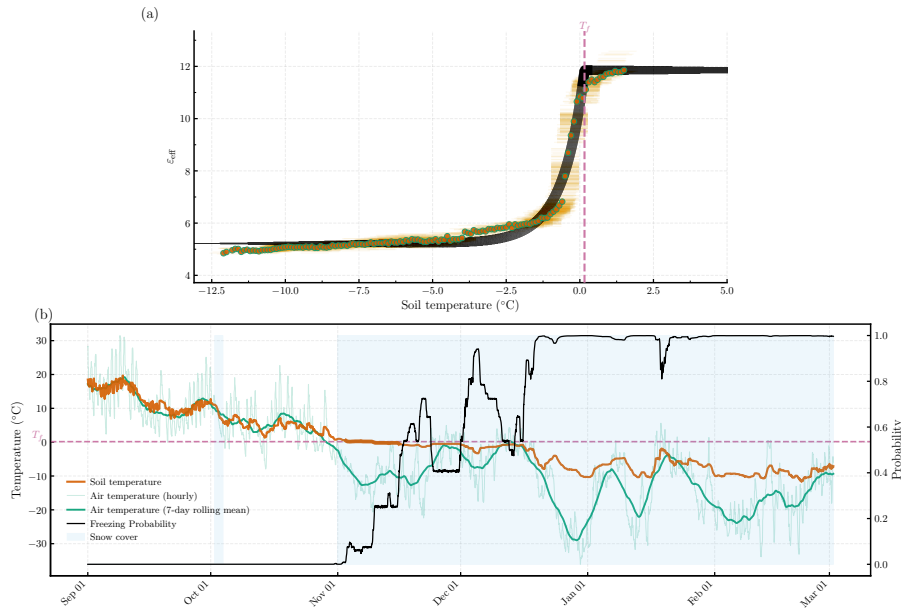


**Figure 6.** Fitted SFCC (a) and corresponding time series of soil temperature, snow cover, and freezing probability (b) for the BJ06-EC17 site in the Baie James-Kenaston network, an eastern boreal forest site. Vertical lines in (a) indicate  $T_f$  (freezing point) and  $T_{res}$  (residual temperature). The prolonged transitional states highlight the zero-curtain effect. The site's location can be found through an interactive map hosted on GitHub: Soil-Temperature-Permittivity-Monitoring-Sites.

classified as “unfrozen” and 36% as “frozen,” leading to smaller and more balanced misclassification. This analysis confirms that the temperature-based method systematically reallocates transitional days into binary categories, and that the direction and magnitude of these biases vary across ecological regions due to differing soil and climate conditions.

Confusion matrix comparing SFCC-based soil state classification (used as the reference) with the temperature-based method across different networks in various land cover types. The analysis is based on daily classifications from October 1st to June 1st.

#### 490 4 Discussion

The presence and behavior of liquid water, and consequently the shape of the SFCC, are influenced by numerous interrelated factors. Our results were generally consistent with the physical factors affecting SFCC shape, including soil mineral composition, particle size, plasticity, initial water content, dry density, solute concentration, freezing rate, confining stress, and freeze-thaw history (Chai et al., 2018; Bi et al., 2023a, b, and references therein). The freezing point ( $T_f$ ) decreases as initial water content decreases. For example, Zhang et al. (2019) found that decreasing soil water content from 37.60% to 14.52% lowered  $T_f$  from  $-0.06^\circ\text{C}$  to  $-0.75^\circ\text{C}$ . A similar pattern emerges in our results, where eastern boreal forest sites, characterized by higher initial

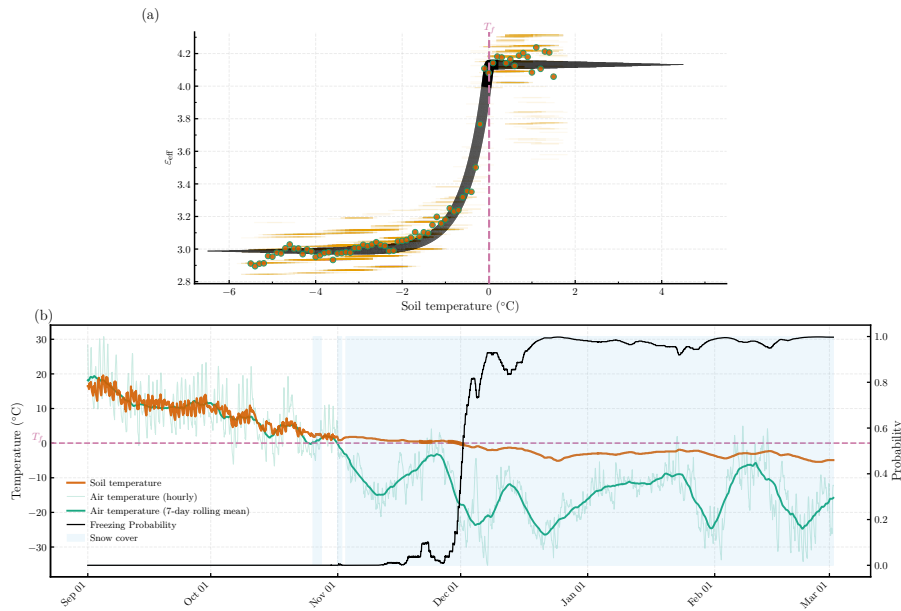


**Figure 7.** Similar to Fig. 86, but for the FM403-BT17 site in the Montmorency Forest-Candle Lake network, an eastern (western boreal forest site located at the transition between boreal and temperate forests). The site experienced two freeze-thaw events during the year, as captured by our SFCC model, with prolonged transitional states reflecting the zero curtain effect.

moisture (indicated by higher  $\epsilon_{\text{ice}}$ ), display higher  $T_f$  than the drier western boreal sites. Soil texture also influences the SFCC. Fine-grained soils show greater freezing point depression and gradual changes in liquid water content, while coarse-grained soils exhibit rapid water loss during freezing (Tian et al., 2014; Zhang et al., 2019; Bi et al., 2023b). This contrast is evident at the Kenaston network, where higher clay content correlates with lower  $T_{\text{res}}$  and a more gradual freezing transition. Additionally, the freezing rate, by altering pore ice formation dynamics, solute distribution, and ice grain size, can affect both the slope and curvature of the SFCC (Watanabe and Osada, 2017). In a natural setting, the freezing rate is primarily driven by decreases in ambient (air) temperature. Networks with wetter soils or limited insulating organic layers—much like in controlled laboratory conditions such as BJ and LR FM and CP (wet), and GR, TV, (with thin organic layers)—yet it is further modulated by the presence of vegetation and snow cover, thus complicating efforts to disentangle the specific effects of air temperature on the SFCC. For instance, in eastern boreal forest sites, abundant snow and insulating moss-lichen cover prolong the zero-curtain period, allowing soil temperatures to remain near the freezing point even when air temperatures plummet below  $-30^{\circ}\text{C}$ . exhibited higher  $b$  values ( $b > 3$ ), indicating sharper freezing transitions driven by abundant capillary water and/or faster freezing rates. In contrast, finer-textured or drier networks, such as KN and BT, showed smaller  $b$  values ( $b < 1.5$ ), reflecting more gradual phase transitions. Despite recognizing these controlling factors, fully disentangling their individual contributions within a natural, open-system environment is inherently challenging. Multiple drivers operate simultaneously and interact nonlinearly, making it difficult to isolate each parameter's effect. Crucially, however, our primary objective was not to develop

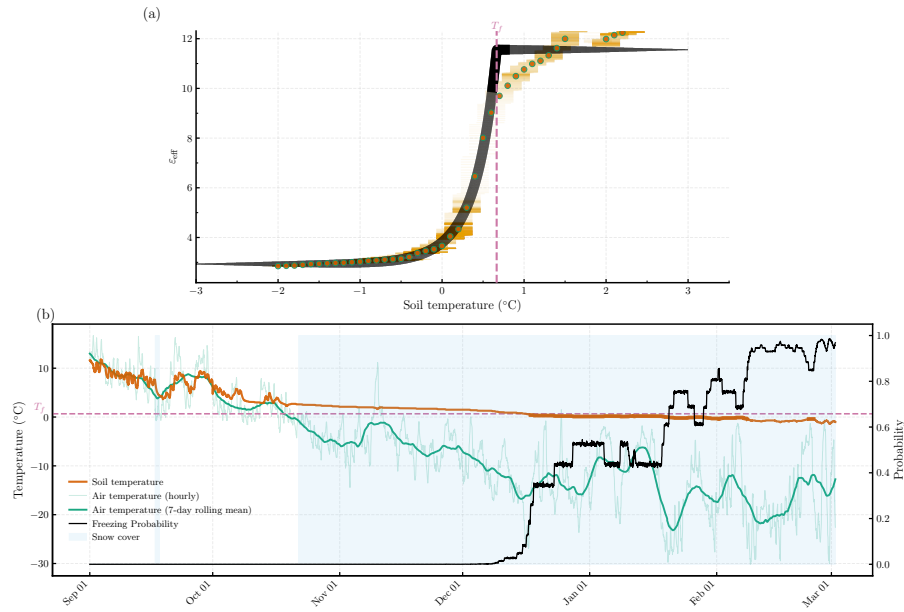


**Figure 8.** Similar to Fig. 86, but for the BT17-BJ01 site in the Candle Lake Baie-James network, a western (eastern boreal forest site). The more extensive freezing reflects drier conditions and lack of insulation compared to eastern sites, with some transitional states present.

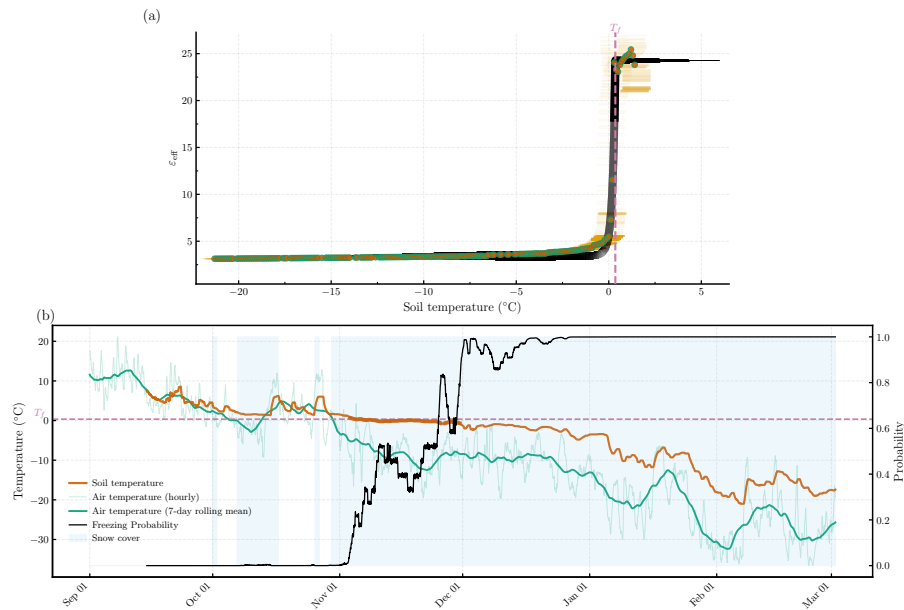


**Figure 9.** Similar to Fig. 86, but for the GR01 site in the George River network, a tundra site. Sharp and rapid freezing transitions result in minimal transitional periods.

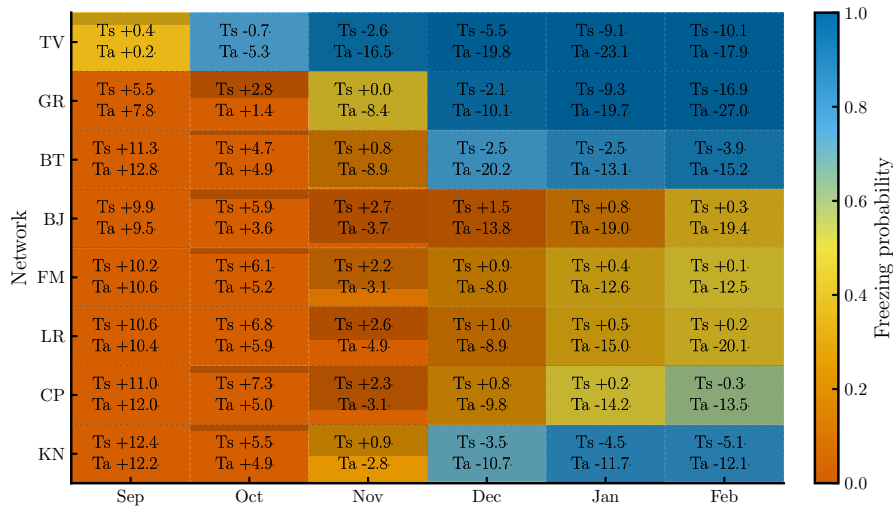


**Figure 10.** Similar to Fig. 8, but Monthly mean freezing probability for the EC17 site in the Kenaston each network, a prairie site. Pronounced fluctuations in Numbers within cells indicate monthly mean soil temperature are observed and air temperatures ( $T_s$ , likely due to minimal  $T_a$ ; °C), while the semi-transparent black fill of each cell represents the monthly mean snow cover and absence of vegetation, which reduce insulation and increase susceptibility to air temperature fluctuations (%).

Heatmap showing the monthly average of the probability of frozen ground for all sites within each network over the entire data period. This visualization highlights regional freeze-thaw patterns: tundra remains frozen longest, prairies freeze earlier but thaw faster due to minimal snow and vegetation, and the eastern boreal forest retains transitional states, indicating incomplete freezing from high water retention and snow insulation.

a universal SFCC model. Instead, we aimed to demonstrate how SFCCs constructed in permittivity-temperature space can enhance the understanding of soil freeze-thaw behavior under real-world conditions. Attempting to explain every observed SFCC from in situ measurements alone is neither feasible nor necessary. Instead, our approach involves fitting individual SFCCs to each freeze-thaw event, embracing their site- and event-specific nature. This strategy avoids the pitfalls of using averaged parameters (such as those in Table ??) or assuming a one-size-fits-all model. It's important to note that the averaged parameters presented in Table ?? should not be used as universal values to determine soil state from temperature data alone. While we can identify general trends and influencing factors, each SFCC must ultimately be interpreted within its unique environmental and soil context. Differences in soil freezing across the networks primarily reflect the combined effects of insulation and moisture rather than air temperature alone. Eastern boreal networks (BJ, FM, LR, and CP) remained largely unfrozen throughout winter due to thicker moss and organic layers, denser canopy cover, and higher soil moisture. These features collectively buffer ground heat loss, dampen temperature fluctuations, prolong the zero curtain phase, and keep the soil in a transitional state for extended periods. This interpretation aligns with modeling results from boreal forests in eastern Canada, where soils were shown to remain near 0°C throughout winter despite mean air temperatures around -16°C (Oogathoo et al., 2022; Lawrence et al., 2008). Such multilayer insulation reduces conductive and radiative heat exchange

530 between the atmosphere and the soil, thereby limiting frost penetration even under severe cold conditions. In contrast, BT—a dry boreal network with sparse vegetation and thin organic horizons—and KN, which lacks vegetation and organic cover, exhibited earlier and deeper freezing. Tundra networks (GR and TV) experienced prolonged freezing driven by extreme cold and minimal insulation; soil freezing began almost immediately after air temperatures fell below 0°C, although GR’s higher soil moisture delayed freeze onset relative to TV.

535 A major source of systematic error in permittivity-based sensors is the volume mismatch between the permittivity-sensing domain and the temperature-sensing thermistor (Pardo Lara et al., 2020, 2021). As shown by Pardo Lara et al. (2021), this mismatch can lead to apparent hysteresis and positive freezing-point depression artifacts, where permittivity sensors detect freezing before the thermistor. This occurs because permittivity sensors integrate over a larger, water-biased volume—one that shrinks in wetter soils—while thermistors measure temperature within a much smaller, localized, and water-independent zone (Hansson and Lundin, 2006; Logsdon, 2009; Pardo Lara et al., 2021). Sensor geometry also plays a role. The thermistor in the TEROS12 is embedded in the central needle, minimizing spatial offset, while in the HydraProbe it is located in the base plate. The CS616 lacks a built-in thermistor, requiring external placement, which can exacerbate mismatch effects. 540 However, in our analysis (Fig. 5), approximately 90% of  $T_f$  values from HydraProbe and all from TEROS12 and CS616 were within the respective sensor uncertainty ranges ( $\pm 2\sigma$  °C) which make our  $T_f$  values within the expected uncertainty bounds of the sensors. This suggests that while volume mismatch may contribute to variability in  $T_f$ , it does not appear to introduce significant systematic bias in our study. However, in our analysis (Fig. 5), approximately 90% of  $T_f$  values from HydraProbe and all from TEROS12 and CS616 fell within the respective sensor uncertainty ranges ( $\pm 2\sigma$  °C), indicating that 545 our  $T_f$  estimates are within the expected uncertainty bounds of the sensors. This suggests that although volume mismatch may contribute to bias in  $T_f$ , it does not result in a significant systematic bias in our study.

One key limitation of this study, as well as any attempt to construct SFCCs from in situ measurements, lies in the assumption that the total water content remains equal to the pre-freezing water content throughout the freezing period (He and Dyck, 2013). In an open system, soil moisture can fluctuate at any time due to rainfall events, intermittent snowmelt, other hydrological inputs, or water redistribution during freezing. This particularly makes identifying a stable “initial” water content (or corresponding  $\epsilon_{\text{eff}}$ ) particularly challenging. However, we found that averaging the permittivity within a small temperature range (e.g.,  $\sigma_T$  °C to 2°C, where  $\sigma_T$  °C to 2°C, where  $\sigma_T$  represents the instrument-specific temperature uncertainty) before the onset of sustained cooling provides a reasonable proxy for the initial moisture conditions. Nevertheless, our results indicate that under freezing conditions—before major thawing or significant water inputs—this assumption holds reasonably well, allowing us to 555 accurately reconstruct  $\epsilon_{\text{eff}}$  from the fitted SFCC. This, in turn, lends credibility to using the derived SFCC parameters to define soil states. Although this approach may introduce some uncertainties, it is both practical and effective under most natural conditions. Integrating air temperature measurements can help address certain complexities. For instance, a concurrent rise in air temperature above zero and an increase in permittivity may indicate external water inputs (e.g., snowmelt) that violate our assumption. The thawing cycles, however, were not analyzed in this study because constructing 560 the STCC from in situ measurements is not reliably feasible. During thawing, snowmelt and rainfall introduce additional water into the soil, violating the constant total water content assumption required for curve development. Another practical challenge

in applying the SFCC ~~approach~~-in situ is identifying distinct freezing and thawing periods. In controlled laboratory settings, these phases are straightforward to define due to precisely managed temperature profiles. In natural environments, however, air temperatures fluctuate continuously—often with pronounced diurnal cycles—leading to brief or incomplete ~~freeze-thaw~~ freeze-thaw events that are difficult to isolate. These fluctuations are particularly common during the fall and spring shoulder seasons, precisely when soils transition between unfrozen and frozen states. Notably, these transitional periods also provide the critical data needed for deriving  ~~$T_f$  and  $b$~~   $T_f$  and  $b$ , making SFCC construction even more challenging. For practical purposes and to improve the reliability of SFCC fitting, we recommend focusing on the main, more sustained freezing ~~and thawing periods~~, periods while disregarding minor, short-lived fluctuations near  $0^{\circ}\text{C}$ . Although this approach may exclude some small-scale ~~freeze-thaw~~ freeze-thaw ~~freezing~~ cycles, prioritizing the most clearly defined ~~freeze-thaw~~ freeze-thaw phases balances the complexities of natural systems with the need for practical, reliable SFCC parameter estimation. Another challenge encountered during SFCC curve fitting arose when freezing progressed rapidly. The limited temporal resolution of the sensors restricted the number of observations within the transitional zone, reducing the model's ability to resolve steep transitions and increasing the uncertainty in the estimated  $b$  values. Consequently, the bootstrap confidence intervals of  $b$  widened systematically with increasing  $b$  (Fig. 5).

For seasonally frozen ground monitoring, sensors that measure both soil temperature and permittivity are essential. The HydraProbe is advantageous as it directly measures permittivity components, while the ~~TEROS-12~~ TEROS12, despite requiring empirical conversion, offers exceptional energy efficiency. The CS616 is less suitable due to its lack of integrated temperature measurement, undefined permittivity conversion, and poor reliability in cold conditions observed at our ~~Chapleau site~~ CP network. We did not perform site- or sensor-specific calibrations for permittivity or temperature, but the sensors ~~used—TEROS-12~~ used—TE HydraProbe, and CS616—have been extensively validated and shown to perform reliably across diverse soil conditions (Seyfried and Murdock, 2004; Kelleners et al., 2005; Hansson and Lundin, 2006; Cominelli et al., 2024; Pardo Lara et al., 2021). Electrical conductivity (EC) is the most influential factor affecting dielectric sensor accuracy. Increased EC elevates the imaginary permittivity component, leading to signal attenuation and overestimated permittivity values (Seyfried et al., 2005). However, EC values at our sites were generally low—below ~~0.03~~ 0.03  $\text{S m}^{-1}$  in boreal and tundra regions (Fig. S1) and below ~~0.20~~ 0.2  $\text{S m}^{-1}$  in ~~Kenaston~~ KN's top 20 cm (Tetlock et al., 2019)—well within acceptable thresholds (~~0.05–0.14~~ 0.05–0.14  $\text{S m}^{-1}$  depending on the sensor). Permittivity for ~~TEROS-12~~ TEROS12 and CS616 was derived from raw sensor output using manufacturer-recommended or physically based models. For CS616, we applied the formulation by Kelleners et al. (2005), using generalized calibration coefficients from prior studies (Kelleners et al., 2005; Logsdon, 2009; Hansson and Lundin, 2006). While this may introduce minor biases, the impact on ~~freeze-thaw~~ freeze-thaw ~~freezing cycle~~ detection is negligible. For ~~TEROS-12~~ TEROS12, we used a third-order polynomial to convert frequency to permittivity (see Equation A2), though underestimation has been reported in saturated conditions (Cominelli et al., 2024; Fragkos et al., 2024). This is unlikely to affect our analysis, as saturated soils are rare during freezing periods—except at ~~Montmorency~~ FM, where soil rarely freezes. Importantly, SFCCs can also be constructed directly from raw sensor output, with negligible differences compared to permittivity-based curves (Fig. S2). Both approaches reveal the clear signal drop needed to identify freezing transitions. Soil texture and organic matter may also affect permittivity measurements (Seyfried and Murdock, 2004; Seyfried et al., 2005), but most sites exhibit low

clay and organic content, with only a few exceptions in ~~Kenaston and Montmorency~~ KN and FM. Overall, the permittivity uncertainty is approximately ~~1–2~~ 1–2 units for CS616 and ~~TEROS 12~~ TEROS12, and about ~~0.1–0.2~~ 0.1–0.2 units for the HydraProbe—values that are well below the typical permittivity shifts observed during soil freezing and thawing. As long as a discernible permittivity change occurs, the SFCC fitting method can reliably identify the ~~freeze–thaw~~ freezing transition. In rare instances where the change is too subtle—e.g., below the measurement uncertainty threshold—the curve-fitting algorithm fails to converge, and such data are automatically excluded from further analysis. Importantly, ~~our detection~~ the SFCC approach is based on the relative change in permittivity with temperature rather than the absolute permittivity values, meaning that minor calibration errors or site-specific variability do not compromise our ability to detect meaningful ~~freeze–thaw events~~ freezing events. Furthermore, sensor measurement uncertainty ( $\sigma_T$  and  $\sigma_\epsilon$ ) was explicitly propagated through Monte Carlo simulations in all probabilistic analyses, ensuring that parameter estimation and freezing probabilities reflect the true uncertainty associated with the sensors.

~~A major source of systematic error in permittivity-based sensors is the volume mismatch between the permittivity-sensing domain and the temperature-sensing thermistor (Pardo Lara et al., 2020, 2021). As shown by Pardo Lara et al. (2021), this mismatch can lead to apparent hysteresis and positive freezing-point depression artifacts, where permittivity sensors detect freezing before the thermistor. This occurs because permittivity sensors integrate over a larger, water-biased volume—one that shrinks in wetter soils—while thermistors measure temperature within a much smaller, localized, and water-independent zone (Hansson and Lundin, 2006; Logsdon, 2009; Pardo Lara et al., 2021). Sensor geometry also plays a role. The thermistor in the TEROS 12 is embedded in the central needle, minimizing spatial offset, while in the HydraProbe it is located in the base plate. The CS616 lacks a built-in thermistor, requiring external placement, which can exacerbate mismatch effects. In our analysis (Fig. ??), approximately 75% of  $T_f$  values from HydraProbe and 50% from TEROS 12 and CS616 were within the respective sensor uncertainty ranges ( $\pm 0.3^\circ\text{C}$  and  $\pm 0.5^\circ\text{C}$ ). Rather than dismissing these positive  $T_f$  values as sensor error, we interpret them as systematic biases resulting from volume mismatch. As they still reflect the relative permittivity change associated with freezing, we consider them informative and include them in our analysis.~~

~~Bootstrapped estimates of  $T_f$  and their 95% confidence intervals for individual freezing cycles. Cycles from sensors with higher temperature uncertainty ( $0.5^\circ\text{C}$ ; e.g., TEROS 12 and CS616) are shown in red, while those from lower uncertainty sensors ( $0.3^\circ\text{C}$ ; e.g., HydraProbe) are shown in grey. Dashed vertical lines at  $0.3^\circ\text{C}$  and  $0.5^\circ\text{C}$  represent one standard deviation ( $\sigma$ ) of the expected uncertainty bounds for each sensor type.~~

~~By comparing the number of frozen days determined using only soil temperature measurements with those derived from our SFCC-based method, we found that the traditional threshold-based approach substantially overestimates the duration of frozen ground. This result underscores the importance of revisiting conventional monitoring practices and reaffirms that proper frozen ground monitoring sites should include soil moisture sensors. Furthermore, relying solely on temperature fails to capture extensive transitional periods, which can be comparable in length to the fully frozen intervals. In light of these findings, we recommend moving away from the notion of a single ‘frozen period’ defined by consecutive frozen days, and instead adopting a more detailed approach that quantifies the number of individual frozen~~

## 5 Conclusions

This study applied an SFCC in permittivity–temperature space to enable robust monitoring of frozen ground states using standard dielectric sensors, ~~transitional, and unfrozen days. Such a perspective provides a dynamic and accurate representation of soil~~ without the calibration challenges inherent in estimating liquid water content. The key insight from our multi-network analysis is that variations in freezing behavior are dominated by local ground surface properties rather than regional air temperature patterns. Importantly, the transitional (partially frozen) state accounts for the majority of the freezing season in eastern boreal networks and persists for at least one month even in western boreal and tundra networks—dynamics that binary frozen/unfrozen classifications fail to capture. These findings reinforce that air temperature alone cannot predict frozen ground extent, demonstrating that remote sensing products and land surface models must account for spatial variations in ground surface properties to accurately represent freeze-thaw behavior, ~~acknowledging the frequent transitions and short-term fluctuations that occur in natural settings. This finer-scale approach more closely aligns with the actual processes taking place in the soil, allowing for improved monitoring and understanding of seasonally frozen ground conditions.~~

This study introduces a new framework for seasonally frozen ground monitoring that moves beyond the traditional binary classification approach, offering a more nuanced understanding of soil freeze-thaw dynamics at regional scales. The practical value of this approach lies in its compatibility with widely deployed sensor networks and its systematic, straightforward methodology for constructing SFCCs from in situ measurements. Numerous soil monitoring networks across cold regions (e.g., RISMA, SNOTEL, AmeriFlux) already measure both soil temperature and dielectric permittivity. These existing infrastructures could readily adopt the methodology presented in this study to monitor seasonally frozen ground. This is particularly important given the rapid warming of high-latitude regions and the need for ground-truth evaluation of satellite-based freeze-thaw products, which currently rely primarily on air or soil temperature observations for training and evaluation (Rautiainen et al., 2025; Donahue et al., 2025). By integrating in situ soil temperature and permittivity measurements through an SFCC model, we can now quantify the degree of soil freezing and identify crucial transitional states—a capability particularly valuable for understanding shoulder season processes and carbon flux dynamics. This advancement addresses a critical gap in cold regions science, where accurate characterization of soil states directly impacts our understanding of hydrological processes, ecosystem responses, and carbon cycling. The framework’s ability to detect and quantify transitional states, which we found can persist as long as fully frozen periods, has significant implications for improving climate models, particularly their representation of shoulder season biogeochemical processes. Additionally, this methodology provides a robust foundation for validating and improving remote sensing products, potentially enabling more accurate regional and global assessments of frozen ground conditions. Looking forward, this approach opens new avenues for integrating ground-based observations with satellite data, ultimately advancing our ability to monitor and predict cold region responses to climate change.

## Appendix A: Sensor Details

### A1 CS616 (Campbell Scientific)

The CS616 water content reflectometer measures soil dielectric permittivity by recording the period (in microseconds) of a square-wave oscillation. This oscillation is generated by an electromagnetic pulse that travels along the sensor's 30 cm stainless steel rods, reflects off their ends, and returns to the circuit board to trigger the next pulse. Since the wave velocity depends on the dielectric properties of the surrounding medium, the measured period is directly related to the effective relative permittivity ( $\epsilon_{\text{eff}}$ ). A physically based equation derived by Kelleners et al. (2005) can be used to convert the raw output to  $\epsilon_{\text{eff}}$ :

$$\epsilon_{\text{eff}} = \left( \frac{(t - 2t_d)c}{4L} \right)^2 \quad (\text{A1})$$

where  $t = \tau/S_t$  is the scaled time period (with  $S_t = 1024$  and  $\tau$  the temperature-corrected raw output in seconds),  $t_d$  is the delay time correction (commonly  $5.4 \times 10^{-9}$  s),  $L$  is the effective rod length (typically 0.261 m for the CS616), and  $c$  is the speed of light in a vacuum ( $3 \times 10^8$  m/s) (Hansson and Lundin, 2006; Kelleners et al., 2005; Logsdon, 2009). Although  $L$  and  $t_d$  can vary slightly between CS616 probes, studies have shown minimal variability (Kelleners et al., 2005; Hansson and Lundin, 2006; Logsdon, 2009). These generalized constants yield acceptable permittivity estimates when sensor-specific calibration is not feasible. Validation against standard reference fluids showed excellent agreement ( $R^2 > 0.99$ ), and comparisons with TDR, HydraProbe, and Topp's model confirm reliable performance across soils. The accuracy of the CS616 may decline in soils with high EC ( $>0.05 > 0.05$  S  $\text{m}^{-1}$ ), clay content ( $>30\%$ ), or organic matter ( $>5 > 5\%$ ) due to signal attenuation and delayed pulse detection. However, the CS616's relatively high operating frequency ( $\sim 175$  MHz) reduces sensitivity to dispersive effects. The CS616's sensing volume averages permittivity over a non-uniform electric field, which is biased toward wetter zones. While this may slightly inflate permittivity in heterogeneous soils, it helps reduce the influence of small-scale spatial variability. While the CS616 does not measure soil temperature directly, it can be paired with the CS109SS-L sensor for temperature measurements. The CS109SS-L operates over a temperature range of  $-40^\circ\text{C}$  to  $+70^\circ\text{C}$ , with an accuracy of  $\pm 0.60 \pm 0.60^\circ\text{C}$  from  $-40^\circ\text{C}$  to  $-20^\circ\text{C}$  and  $\pm 0.49 \pm 0.49^\circ\text{C}$  from  $-20^\circ\text{C}$  to  $+70^\circ\text{C}$ .

### A2 ~~TEROS-12~~ TEROS12 (METER Group)

The ~~TEROS-12~~ TEROS12 (METER Group, Inc.) uses capacitance-based technology to estimate soil dielectric permittivity. Operating at  $7070$  MHz, it sends an oscillating signal through three  $5.555$  cm prongs, which act as a capacitor with the surrounding soil as the dielectric medium. The sensor measures the charge time, which reflects the soil's dielectric properties, and outputs a scaled frequency (RAW) value. This value is converted to  $\epsilon_{\text{eff}}$  using a third-order polynomial calibration equation provided in the manual:

$$\epsilon_{\text{eff}} = (2.887 \times 10^{-9} \times \text{RAW}^3 - 2.080 \times 10^5 \times \text{RAW}^2 + 5.276 \times 10^2 \times \text{RAW} - 43.39)^2 \quad (\text{A2})$$

690 The sensor's reported accuracy is  $\pm 1$  unit for  $\epsilon_{\text{eff}} \in [1, 40]$  and  $\pm 15\%$  for values above ~~40~~40. However, studies have shown that the TEROS 12 can systematically underestimate dielectric permittivity in highly saturated soils and exhibits increased sensitivity under saline conditions (Cominelli et al., 2024; Fragkos et al., 2024). While the manufacturer lists a nominal sensing volume of approximately  $1010 \text{ cm}^3$ , experimental evaluations report a smaller effective volume in moist sand (approximately  $423 \text{ cm}^3$ ) and a further reduction in pure water (down to ~~848~~4  $\text{cm}^3$ ). The sensor also demonstrates strong thermal stability, with  
 695 temperature-induced changes in permittivity typically remaining below 1 unit across the ~~10–40~~10–40  $^{\circ}\text{C}$  range (Cominelli et al., 2024). The TEROS 12 also incorporates an internal thermistor embedded in the central needle to measure temperature. These temperature readings range from  $-40$  to ~~60~~60  $^{\circ}\text{C}$ , with an accuracy of  ~~$\pm 0.5^{\circ}\text{C}$~~  $\pm 0.5^{\circ}\text{C}$  from  $-40$  to  ~~$0^{\circ}\text{C}$~~  $0^{\circ}\text{C}$  and  ~~$\pm 0.3^{\circ}\text{C}$~~  $\pm 0.3^{\circ}\text{C}$  from  $0$  to  ~~$60^{\circ}\text{C}$~~  $60^{\circ}\text{C}$ .

### A3 HydraProbe (Stevens Water)

700 The HydraProbe (Stevens Water Monitoring Systems) uses coaxial impedance dielectric reflectometry to measure the real and imaginary components of complex dielectric permittivity. It features a coaxial waveguide with four stainless steel tines (~~0.30.3~~0.30.3 cm diameter, ~~5.75.7~~5.75.7 cm length) arranged in a circle around a central tine, protruding from a ~~4.24.2~~4.24.2 cm metal base plate. A ~~5050~~5050 MHz signal is transmitted through the tines, and the sensor analyzes the amplitude ratio of incident to reflected waves to solve Maxwell's equations. This allows separate estimation of the real ( $\epsilon'_r$ ) and imaginary ( $\epsilon''_r$ ) components of  $\epsilon_{\text{eff}}$ , computed  
 705 as follows (von Hippel, 1966; Topp et al., 1980):

$$\epsilon_{\text{eff}} = \frac{\epsilon'_r}{2} \left( 1 + \sqrt{1 + \left( \frac{\epsilon''_r}{\epsilon'_r} \right)^2} \right) \quad (\text{A3})$$

Laboratory tests confirm that the HydraProbe provides precise and consistent permittivity measurements, with inter-sensor variability typically below  ~~$\pm 0.5$  units and  $< 1\%$~~  $\pm 0.5$  units and  $< 1\%$  coefficient of variation in fluids (Seyfried and Murdock, 2004). It performs reliably up to soil EC values of  ~~$\sim 0.14 \text{ S m}^{-1}$~~  $\sim 0.14 \text{ S m}^{-1}$ , beyond which accuracy declines. Loss tangent  
 710 values above  $\sim 1.45$  lead to unstable readings. Despite lacking internal temperature correction, temperature effects are minor—e.g.,  $\sim 0.0077 \text{ units}^{\circ}\text{C}^{-1}$  in air and up to  ~~$\pm 0.06 \text{ m}^3 \text{ m}^{-3}$~~  $\pm 0.06 \text{ m}^3 \text{ m}^{-3}$  in saturated clay soils over a ~~40–40~~40–40  $^{\circ}\text{C}$  range. The nominal sensing volume of the HydraProbe is approximately  ~~$4.0 \times 10^4 \text{ mm}^3$~~  $4.0 \times 10^4 \text{ mm}^3$ , but it can expand up to  ~~$\sim 3.5 \times 10^5 \text{ mm}^3$~~  $\sim 3.5 \times 10^5 \text{ mm}^3$  depending on soil conditions. The effective sensing volume increases in soils with lower permittivity—such as dry or frozen soils—and contracts in wetter soils with higher permittivity. Temperature is measured via a thermistor in contact  
 715 with the base plate, with a range of  ~~$-40^{\circ}\text{C}$  to  $+75^{\circ}\text{C}$~~  $-40^{\circ}\text{C}$  to  $+75^{\circ}\text{C}$ , an accuracy of  ~~$\pm 0.3^{\circ}\text{C}$~~  $\pm 0.3^{\circ}\text{C}$ , and a resolution of  ~~$0.1^{\circ}\text{C}$~~  $0.1^{\circ}\text{C}$ .

## Appendix B: Instrumentation Setup

Figure A1 illustrates the insertion depths and orientations of each probe (CS616, HydraProbe, and ~~TEROS-12~~TEROS12), along with their standard needle lengths. Accompanying the schematic are actual images of the probes to enhance visual recognition and familiarity with their designs.

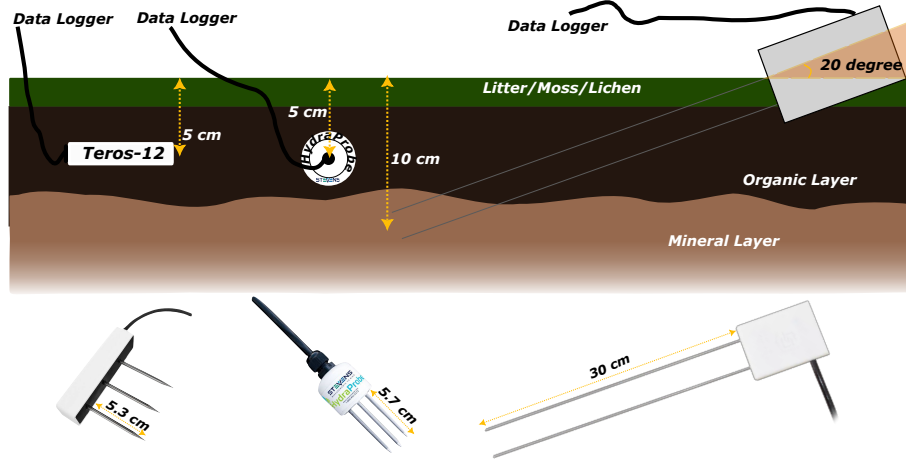


**Figure A1.** Instrumentation setup for soil moisture probes (CS616, HydraProbe, and ~~TEROS-12~~TEROS12), with a schematic and corresponding probe images.

## Appendix B: Derivation of ~~Bai et al.~~Bai et al.'s Model in Permittivity-Temperature Space

In this section, we present the detailed steps that transform the Eq. (1) from liquid water content-soil temperature space into permittivity-soil temperature space. The resulting equation expresses the soil's effective permittivity as a function of soil temperature, as shown in Eq.( 4).

725 **B1 For  $T > T_{\text{soil}}$**

The simplified form of Eq.( 3) is:

$$\theta_{lw} = A\varepsilon_{\text{eff}}^{\alpha} + B - \theta_{\text{ice}}C \quad (\text{B1})$$

where  $A$ ,  $B$ , and  $C$  are defined as:

$$A = \frac{1}{\varepsilon_{lw}^{\alpha} - \varepsilon_{\text{air}}^{\alpha}}, \quad (\text{B2})$$

$$730 \quad B = \frac{(n-1)\varepsilon_{\text{soil}}^{\alpha} - n\varepsilon_{\text{air}}^{\alpha}}{\varepsilon_{\text{lw}}^{\alpha} - \varepsilon_{\text{air}}^{\alpha}}, \quad (\text{B3})$$

$$C = \frac{\varepsilon_{\text{ice}}^{\alpha} - \varepsilon_{\text{air}}^{\alpha}}{\varepsilon_{\text{lw}}^{\alpha} - \varepsilon_{\text{air}}^{\alpha}}. \quad (\text{B4})$$

For  $T > T_{\text{soil}}$ , we know that  $\theta_{\text{ice}} = 0$ . Therefore, we have:

$$\theta_{\text{lw}} = A\varepsilon_{\text{eff}}^{\alpha} + B \quad (\text{B5})$$

Additionally, the liquid water content  $\theta_{\text{int}}$  is given by:

$$735 \quad \theta_{\text{int}} = A\varepsilon_{\text{int}}^{\alpha} + B \quad (\text{B6})$$

Thus, for  $T > T_{\text{soil}}$ :

$$\varepsilon_{\text{eff}} = \varepsilon_{\text{int}} \quad (\text{B7})$$

## **B2 For $T \leq T_{\text{soil}}$**

For  $T \leq T_{\text{soil}}$ , we can express  $\theta_{\text{ice}}$  in terms of  $\theta_{\text{int}}$  and  $\theta_{\text{res}}$ :

$$740 \quad \theta_{\text{ice}} = \theta_{\text{int}} - \theta_{\text{lw}} \quad (\text{B8})$$

**Step 1:** Substitute  $\theta_{\text{ice}}$  into  $\theta_{\text{res}}$ :

$$\theta_{\text{res}} = A\varepsilon_{\text{res}}^{\alpha} + B - (\theta_{\text{int}} - \theta_{\text{res}})C \quad (\text{B9})$$

**Step 2:** Simplify the equation:

$$\theta_{\text{res}} = A\varepsilon_{\text{res}}^{\alpha} + B - \theta_{\text{int}}C + \theta_{\text{res}}C \quad (\text{B10})$$

745 **Step 3:** Bring like terms together:

$$\theta_{\text{res}}(1 - C) = A\varepsilon_{\text{res}}^{\alpha} + B - \theta_{\text{int}}C \quad (\text{B11})$$

**Step 4:** Solve for  $\theta_{\text{res}}$ :

$$\theta_{\text{res}} = \frac{A\varepsilon_{\text{res}}^{\alpha} + B - \theta_{\text{int}}C}{1 - C} \quad (\text{B12})$$

**Step 5:** Similarly, for  $\theta_{\text{lw}}$ :

$$750 \quad \theta_{\text{lw}} = \frac{A\varepsilon_{\text{eff}}^{\alpha} + B - \theta_{\text{int}}C}{1 - C} \quad (\text{B13})$$

**Step 6:** Substitute these expressions into the ~~model from Bai et al. (2018)~~ Bai et al.'s model for  $T \leq T_{\text{soil}}$ :

$$\theta_{\text{lw}} = (\theta_{\text{int}} - \theta_{\text{res}})e^{b(T_{\text{soil}} - T_f)} + \theta_{\text{res}} \quad (\text{B14})$$

**Step 7:** Express  $\theta_{\text{int}} - \theta_{\text{res}}$ :

$$\theta_{\text{int}} - \theta_{\text{res}} = \frac{A(\varepsilon_{\text{int}}^{\alpha} - \varepsilon_{\text{res}}^{\alpha})}{1 - C} \quad (\text{B15})$$

755 **Step 8:** Substitute back and simplify:

$$\frac{A\varepsilon_{\text{eff}}^{\alpha} + B - \theta_{\text{int}}C}{1 - C} = \frac{A(\varepsilon_{\text{int}}^{\alpha} - \varepsilon_{\text{res}}^{\alpha})}{1 - C}e^{b(T_{\text{soil}} - T_f)} + \frac{A\varepsilon_{\text{res}}^{\alpha} + B - \theta_{\text{int}}C}{1 - C} \quad (\text{B16})$$

**Step 9:** Multiply both sides by  $1 - C$  to eliminate denominator:

$$A\varepsilon_{\text{eff}}^{\alpha} + B - \theta_{\text{int}}C = A(\varepsilon_{\text{int}}^{\alpha} - \varepsilon_{\text{res}}^{\alpha})e^{b(T_{\text{soil}} - T_f)} + A\varepsilon_{\text{res}}^{\alpha} + B - \theta_{\text{int}}C \quad (\text{B17})$$

**Step 10:** Subtract common terms from both sides:

$$760 \quad A\varepsilon_{\text{eff}}^{\alpha} = A(\varepsilon_{\text{int}}^{\alpha} - \varepsilon_{\text{res}}^{\alpha})e^{b(T_{\text{soil}} - T_f)} + A\varepsilon_{\text{res}}^{\alpha} \quad (\text{B18})$$

**Step 11:** Divide both sides by  $A$ :

$$\varepsilon_{\text{eff}}^{\alpha} = (\varepsilon_{\text{int}}^{\alpha} - \varepsilon_{\text{res}}^{\alpha})e^{b(T_{\text{soil}} - T_f)} + \varepsilon_{\text{res}}^{\alpha} \quad (\text{B19})$$

Thus, we finally arrive at:

$$\varepsilon_{\text{eff}} = \left( (\varepsilon_{\text{int}}^{\alpha} - \varepsilon_{\text{res}}^{\alpha})e^{b(T_{\text{soil}} - T_f)} + \varepsilon_{\text{res}}^{\alpha} \right)^{\frac{1}{\alpha}} \quad (\text{B20})$$

765 . Scripts used for analysis and plotting, primarily written in Python 3.9, are available upon request from the authors. The dataset used to create the interactive site map is publicly accessible on GitHub (GitHub Repository). The raw sensor outputs, including effective permittivity of bulk soil (computed from the direct raw measurements of the probes), uncalibrated soil moisture data, and soil temperature measurements, along with the final study output (degree of soil freezing), are available upon request for future research applications.

. H.S.: Conceptualization, Methodology, Software, Data Curation, Formal Analysis, Validation, Visualization, Funding Acquisition, Writing  
770 - Original Draft, Writing - Review & Editing. R.P.L.: Methodology, Writing - Review & Editing. A.B.: Supervision, Funding Acquisition, Investigation, Writing - Review & Editing. A.R.: Supervision, Methodology, Funding Acquisition, Investigation, Writing - Review & Editing. A.M.: Investigation, Data Curation, Writing - Review & Editing. C.H.: Investigation, Data Curation, Writing - Review & Editing. B.M.: Investigation, Data Curation, Writing - Review & Editing.

. The contact author has declared that none of the authors has any competing interests.

775 . This study was supported by the Natural Sciences and Engineering Research Council of Canada (NSERC) and the Canadian Space Agency (CSA), as well as the Fonds de recherche du Québec – Nature et technologies (FRQNT) through a Ph.D. scholarship awarded to H.S ([Salmabadi, 2025](#)). We also extend our gratitude to Joshua King, who passed away in February 2023, for his invaluable contributions to this field, particularly for his work on instrumentation in the Trail Valley Creek dataset. We would also like to thank the Centre d'Études Nordiques (CEN) for their logistical support. This work was further supported by contributions from Hydro-Québec, and Environment and  
780 Climate Change Canada. Finally, we acknowledge the invaluable assistance of our colleagues Camille Roy, Alex Gélinas, Azza Gorrab, Esteban Hamel Jomphe, and Kayla Wicks whose help was essential during fieldwork.

. This research was supported by the Fonds de recherche du Québec – Nature et technologies (grant no. 330450; Salmabadi, 2025) and the Canadian Space Agency (grant no. 19FAQCT B19).

## References

- 785 Ala-Aho, P., Autio, A., Bhattacharjee, J., Isokangas, E., Kujala, K., Marttila, H., Menberu, M., Meriö, L.-J., Postila, H., Rauhala, A., Ronkanen, A.-K., Rossi, P. M., Saari, M., Haghighi, A. T., and Kløve, B.: What conditions favor the influence of seasonally frozen ground on hydrological partitioning? A systematic review, *Environmental Research Letters*, 16, 043 008, <https://doi.org/10.1088/1748-9326/abe82c>, 2021.
- Amankwah, S. K., Ireson, A. M., and Brannen, R.: An improved model and field calibration technique for measuring liquid water content in unfrozen and frozen soils with dielectric probes, *Vadose Zone Journal*, 21, e20 225, <https://doi.org/10.1002/vzj2.20225>, 2022.
- 790 Andersland, O. and Ladanyi, B.: *Frozen ground engineering*, John Wiley & Sons, 2003.
- Arndt, K. A., Hashemi, J., Natali, S. M., Schiferl, L. D., and Virkkala, A.-M.: Recent Advances and Challenges in Monitoring and Modeling Non-Growing Season Carbon Dioxide Fluxes from the Arctic Boreal Zone, *Current Climate Change Reports*, 9, 27–40, <https://doi.org/10.1007/s40641-023-00190-4>, 2023.
- 795 Azizi-Rad, M., Guggenberger, G., Ma, Y., and Sierra, C. A.: Sensitivity of soil respiration rate with respect to temperature, moisture and oxygen under freezing and thawing, *Soil Biology and Biochemistry*, 165, 108 488, <https://doi.org/10.1016/j.soilbio.2021.108488>, 2022.
- Bai, R., Lai, Y., Zhang, M., and Yu, F.: Theory and application of a novel soil freezing characteristic curve, *Applied Thermal Engineering*, 129, 1106–1114, <https://doi.org/10.1016/j.applthermaleng.2017.10.121>, 2018.
- Bi, J., Wang, G., Wu, Z., Wen, H., Zhang, Y., Lin, G., and Sun, T.: Investigation on unfrozen water content models of freezing soils, *Frontiers* 800 *in Earth Science*, 10, 1039 330, <https://doi.org/10.3389/feart.2022.1039330>, 2023a.
- Bi, J., Wu, Z., Lu, Y., Wen, H., Zhang, Y., Shen, Y., Wei, T., and Wang, G.: Study on soil freezing characteristic curve during a freezing-thawing process, *Frontiers in Earth Science*, 10, 1007 342, <https://doi.org/10.3389/feart.2022.1007342>, 2023b.
- Bouyoucos, G. and McCool, M. M.: A New Method of Measuring the Concentration of the Soil Solution Around the Soil Particles, *Science*, 42, 507–508, <https://doi.org/10.1126/science.42.1084.507>, 1915.
- 805 C3S: ERA5 hourly data on single levels from 1940 to present, <https://doi.org/10.24381/CDS.ADBB2D47>, 2018.
- Chai, M., Zhang, J., Zhang, H., Mu, Y., Sun, G., and Yin, Z.: A method for calculating unfrozen water content of silty clay with consideration of freezing point, *Applied Clay Science*, 161, 474–481, <https://doi.org/10.1016/j.clay.2018.05.015>, 2018.
- Chen, Y., Zhou, Z., Wang, J., Zhao, Y., and Dou, Z.: Quantification and division of unfrozen water content during the freezing process and the influence of soil properties by low-field nuclear magnetic resonance, *Journal of Hydrology*, 602, 126 719, 810 <https://doi.org/10.1016/j.jhydrol.2021.126719>, 2021.
- Cominelli, S., Rivera, L. D., Brown, W. G., Ochsner, T. E., and Patrignani, A.: Calibration of TEROS 10 and TEROS 12 electromagnetic soil moisture sensors, *Soil Science Society of America Journal*, 88, 2104–2122, <https://doi.org/10.1002/saj2.20777>, 2024.
- Davidson, E. A. and Janssens, I. A.: Temperature sensitivity of soil carbon decomposition and feedbacks to climate change, *Nature*, 440, 165–173, <https://doi.org/10.1038/nature04514>, 2006.
- 815 Decker, K. L. M., Wang, D., Waite, C., and Scherbatskoy, T.: Snow Removal and Ambient Air Temperature Effects on Forest Soil Temperatures in Northern Vermont, *Soil Science Society of America Journal*, 67, 1234–1242, <https://doi.org/10.2136/sssaj2003.1234>, 2003.
- Dobiński, W.: Permafrost active layer, *Earth-Science Reviews*, 208, 103 301, <https://doi.org/10.1016/j.earscirev.2020.103301>, 2020.

- Domine, F., Lackner, G., Sarrazin, D., Poirier, M., and Belke-Brea, M.: Meteorological, snow and soil data (2013–2019) from a herb tundra  
820 permafrost site at Bylot Island, Canadian high Arctic, for driving and testing snow and land surface models, *Earth System Science Data*,  
13, 4331–4348, <https://doi.org/10.5194/essd-13-4331-2021>, 2021.
- Donahue, K., Kimball, J. S., Du, J., Bunt, F., Colliander, A., Moghaddam, M., Johnson, J., Kim, Y., and Rawlins, M. A.: Deep  
learning estimation of northern hemisphere soil freeze-thaw dynamics using satellite multi-frequency microwave brightness temperature  
observations, *Frontiers in Big Data*, 6, 1243 559, <https://doi.org/10.3389/fdata.2023.1243559>, 2023.
- 825 Flerchinger, G. and Pierson, F.: Modeling plant canopy effects on variability of soil temperature and water, *Agricultural and Forest  
Meteorology*, 56, 227–246, [https://doi.org/10.1016/0168-1923\(91\)90093-6](https://doi.org/10.1016/0168-1923(91)90093-6), 1991.
- Fragkos, A., Loukatos, D., Kargas, G., and Arvanitis, K. G.: Response of the TEROS 12 Soil Moisture Sensor under Different Soils and  
Variable Electrical Conductivity, *Sensors*, 24, 2206, <https://doi.org/10.3390/s24072206>, number: 7 Publisher: Multidisciplinary Digital  
Publishing Institute, 2024.
- 830 Fu, Q., Hou, R., Li, T., Jiang, R., Yan, P., Ma, Z., and Zhou, Z.: Effects of soil water and heat relationship under various snow cover during  
freezing-thawing periods in Songnen Plain, China, *Scientific Reports*, 8, 1325, <https://doi.org/10.1038/s41598-018-19467-y>, 2018.
- Gao, H., Nie, N., Zhang, W., and Chen, H.: Monitoring the spatial distribution and changes in permafrost with passive microwave remote  
sensing, *ISPRS Journal of Photogrammetry and Remote Sensing*, 170, 142–155, <https://doi.org/10.1016/j.isprsjprs.2020.10.011>, 2020.
- Gornall, J. L., Jónsdóttir, I. S., Woodin, S. J., and Van Der Wal, R.: Arctic mosses govern below-ground environment and ecosystem processes,  
835 *Oecologia*, 153, 931–941, <https://doi.org/10.1007/s00442-007-0785-0>, 2007.
- Hanes, C. C., Wotton, M., Bourgeau-Chavez, L., Woolford, D. G., Bélair, S., Martell, D., and Flannigan, M. D.: Evaluation of new  
methods for drought estimation in the Canadian Forest Fire Danger Rating System, *International Journal of Wildland Fire*, 32, 836–853,  
<https://doi.org/10.1071/WF22112>, publisher: CSIRO PUBLISHING, 2023.
- Hansson, K. and Lundin, L.-C.: Water Content Reflectometer Application to Construction Materials and its Relation  
840 to Time Domain Reflectometry, *Vadose Zone Journal*, 5, 459–468, <https://doi.org/10.2136/vzj2005.0053>,  
<https://onlinelibrary.wiley.com/doi/pdf/10.2136/vzj2005.0053>, 2006.
- Hayashi, M.: The Cold Vadose Zone: Hydrological and Ecological Significance of Frozen-Soil Processes, *Vadose Zone Journal*, 12, 1–8,  
<https://doi.org/10.2136/vzj2013.03.0064>, 2013.
- He, H. and Dyck, M.: Application of Multiphase Dielectric Mixing Models for Understanding the Effective Dielectric  
845 Permittivity of Frozen Soils, *Vadose Zone Journal*, 12, vzj2012.0060, <https://doi.org/10.2136/vzj2012.0060>,  
<https://onlinelibrary.wiley.com/doi/pdf/10.2136/vzj2012.0060>, 2013.
- Kelleners, T. J. and Norton, J. B.: Determining Water Retention in Seasonally Frozen Soils Using Hydra Impedance Sensors, *Soil Science  
Society of America Journal*, 76, 36–50, <https://doi.org/10.2136/sssaj2011.0222>, 2012.
- Kelleners, T. J., Seyfried, M. S., Blonquist, J. M., Bilskie, J., and Chandler, D. G.: Improved Interpretation of Water Content Reflectometer  
850 Measurements in Soils, *Soil Science Society of America Journal*, 69, 1684–1690, <https://doi.org/10.2136/sssaj2005.0023>, 2005.
- Kersten, M. S.: Thermal Properties of Soils, <https://hdl.handle.net/11299/124271>, 1949.
- Kim, Y., Kimball, J. S., McDonald, K. C., and Glassy, J.: Developing a Global Data Record of Daily Landscape Freeze/Thaw  
Status Using Satellite Passive Microwave Remote Sensing, *IEEE Transactions on Geoscience and Remote Sensing*, 49, 949–960,  
<https://doi.org/10.1109/TGRS.2010.2070515>, 2011.
- 855 Koopmans, R. W. R. and Miller, R. D.: Soil Freezing and Soil Water Characteristic Curves, *Soil Science Society of America Journal*, 30,  
680–685, <https://doi.org/10.2136/sssaj1966.03615995003000060011x>, 1966.

- Kou, X., Jiang, L., Yan, S., Zhao, T., Lu, H., and Cui, H.: Detection of land surface freeze-thaw status on the Tibetan Plateau using passive microwave and thermal infrared remote sensing data, *Remote Sensing of Environment*, 199, 291–301, <https://doi.org/10.1016/j.rse.2017.06.035>, 2017.
- 860 Kozłowski, T.: A semi-empirical model for phase composition of water in clay–water systems, *Cold Regions Science and Technology*, 49, 226–236, <https://doi.org/10.1016/j.coldregions.2007.03.013>, 2007.
- Latifovic, R.: Canada’s land cover, Tech. Rep. 119e, <https://doi.org/10.4095/315659>, edition: version 2015, 2019.
- Lawrence, D. M., Slater, A. G., Romanovsky, V. E., and Nicolsky, D. J.: Sensitivity of a model projection of near-surface permafrost degradation to soil column depth and representation of soil organic matter, *Journal of Geophysical Research: Earth Surface*, 113, 865 2007JF000 883, <https://doi.org/10.1029/2007JF000883>, 2008.
- Lei, D., Yang, Y., Cai, C., Chen, Y., and Wang, S.: The Modelling of Freezing Process in Saturated Soil Based on the Thermal-Hydro-Mechanical Multi-Physics Field Coupling Theory, *Water*, 12, 2684, <https://doi.org/10.3390/w12102684>, 2020.
- Lei, N., Wang, H., Zhang, Y., and Chen, T.: Components of respiration and their temperature sensitivity in four reconstructed soils, *Scientific Reports*, 12, 6107, <https://doi.org/10.1038/s41598-022-09918-y>, 2022.
- 870 Logsdon, S. D.: CS616 Calibration: Field versus Laboratory, *Soil Science Society of America Journal*, 73, 1–6, <https://doi.org/10.2136/sssaj2008.0146>, publisher: Wiley, 2009.
- Loranty, M. M., Abbott, B. W., Blok, D., Douglas, T. A., Epstein, H. E., Forbes, B. C., Jones, B. M., Kholodov, A. L., Kropp, H., Malhotra, A., Mamet, S. D., Myers-Smith, I. H., Natali, S. M., O’Donnell, J. A., Phoenix, G. K., Rocha, A. V., Sonnentag, O., Tape, K. D., and Walker, D. A.: Reviews and syntheses: Changing ecosystem influences on soil thermal regimes in northern high-latitude permafrost 875 regions, *Biogeosciences*, 15, 5287–5313, <https://doi.org/10.5194/bg-15-5287-2018>, 2018.
- MacKinney, A. L.: Effects of Forest Litter on Soil Temperature and Soil Freezing in Autumn and Winter, *Ecology*, 10, 312–321, <https://doi.org/10.2307/1929507>, 1929.
- Mavrovic, A., Pardo Lara, R., Berg, A., Demontoux, F., Royer, A., and Roy, A.: Soil dielectric characterization at L-band microwave frequencies during freeze-thaw transitions, <https://doi.org/10.5194/hess-2020-291>, 2020.
- 880 Mavrovic, A., Sonnentag, O., Lemmetyinen, J., Voigt, C., Rutter, N., Mann, P., Sylvain, J.-D., and Roy, A.: Environmental controls of winter soil carbon dioxide fluxes in boreal and tundra environments, *Biogeosciences*, 20, 5087–5108, <https://doi.org/10.5194/bg-20-5087-2023>, publisher: Copernicus GmbH, 2023.
- Michael W Smith and Tice, A. R.: Measurement of the Unfrozen Water Content of Soils. Comparison of NMR (Nuclear Magnetic Resonance) and TDR (Time Domain Reflectometry) Methods, CRREL Rep. 88-18. U.S. Army Corps of Engineers, Cold Regions Research and 885 Engineering Lab, Hannover, NH., 1988.
- Mikan, C. J., Schimel, J. P., and Doyle, A. P.: Temperature controls of microbial respiration in arctic tundra soils above and below freezing, *Soil Biology and Biochemistry*, 34, 1785–1795, [https://doi.org/10.1016/S0038-0717\(02\)00168-2](https://doi.org/10.1016/S0038-0717(02)00168-2), 2002.
- Montpetit, B., King, J., Meloche, J., Derksen, C., Siqueira, P., Adam, J. M., Toose, P., Brady, M., Wendleder, A., Vionnet, V., and Leroux, N. R.: Retrieval of airborne Ku-Band SAR Using Forward Radiative Transfer Modeling to Estimate Snow Water Equivalent: The Trail 890 Valley Creek 2018/19 Snow Experiment, <https://doi.org/10.5194/egusphere-2024-651>, 2024.
- Montpetit, B., King, J., Toose, P., Berg, A., Pardo Lara, R., Silis, A., and Derksen, C.: TVC Experiment 2018/19: HydraProbe soil stations data, <https://doi.org/https://doi.org/10.5281/zenodo.14611093>, 2025.
- Nikrad, M. P., Kerkhof, L. J., and Häggblom, M. M.: The subzero microbiome: microbial activity in frozen and thawing soils, *FEMS Microbiology Ecology*, 92, fiw081, <https://doi.org/10.1093/femsec/fiw081>, 2016.

- 895 Oogathoo, S., Houle, D., Duchesne, L., and Kneeshaw, D.: Evaluation of simulated soil moisture and temperature for a Canadian boreal forest, *Agricultural and Forest Meteorology*, 323, 109 078, <https://doi.org/10.1016/j.agrformet.2022.109078>, 2022.
- Overduin, P., Kane, D., and Van Loon, W.: Measuring thermal conductivity in freezing and thawing soil using the soil temperature response to heating, *Cold Regions Science and Technology*, 45, 8–22, <https://doi.org/10.1016/j.coldregions.2005.12.003>, 2006.
- Pardo Lara, R., Berg, A. A., Warland, J., and Tetlock, E.: In Situ Estimates of Freezing/Melting Point Depression in Agricultural Soils Using Permittivity and Temperature Measurements, *Water Resources Research*, 56, e2019WR026 020, <https://doi.org/10.1029/2019WR026020>,  
900 \_eprint: <https://onlinelibrary.wiley.com/doi/pdf/10.1029/2019WR026020>, 2020.
- Pardo Lara, R., Berg, A. A., Warland, J., and Parkin, G.: Implications of measurement metrics on soil freezing curves: A simulation of freeze–thaw hysteresis, *Hydrological Processes*, 35, e14 269, <https://doi.org/10.1002/hyp.14269>, 2021.
- Park, H., Launiainen, S., Konstantinov, P. Y., Iijima, Y., and Fedorov, A. N.: Modeling the Effect of Moss Cover on Soil Temperature and Carbon Fluxes at a Tundra Site in Northeastern Siberia, *Journal of Geophysical Research: Biogeosciences*, 123, 3028–3044,  
905 <https://doi.org/10.1029/2018JG004491>, 2018.
- Ping, C. L., Jastrow, J. D., Jorgenson, M. T., Michaelson, G. J., and Shur, Y. L.: Permafrost soils and carbon cycling, *SOIL*, 1, 147–171, <https://doi.org/10.5194/soil-1-147-2015>, 2015.
- Rautiainen, K., Holmberg, M., Cohen, J., Mialon, A., Schwank, M., Lemmetyinen, J., De La Fuente, A., and Kerr, Y.: An operational SMOS soil freeze–thaw product, *Earth System Science Data*, 17, 5337–5353, <https://doi.org/10.5194/essd-17-5337-2025>, 2025.
- Roth, K., Schulin, R., Flühler, H., and Attinger, W.: Calibration of time domain reflectometry for water content measurement using a composite dielectric approach, *Water Resources Research*, 26, 2267–2273, <https://doi.org/10.1029/WR026i010p02267>, 1990.
- Roy, A., Toose, P., Mavrovic, A., Pappas, C., Royer, A., Derksen, C., Berg, A., Rowlandson, T., El-Amine, M., Barr, A., Black, A., Langlois, A., and Sonnentag, O.: L-Band response to freeze/thaw in a boreal forest stand from ground- and tower-based radiometer observations, *Remote Sensing of Environment*, 237, 111 542, <https://doi.org/10.1016/j.rse.2019.111542>, 2020.  
915
- Salmabadi, H.: Development of New Microwave Multi-Sensor Freeze/Thaw Products for Improving Growing Season Monitoring in North America, <https://doi.org/10.69777/330450>, application No.\ 330450, 2025.
- Salmabadi, H., Berg, A., Mavrovic, A., Gorrab ep El Khedhri, A., MacRae, H. C., Hanes, C., and Roy, A.: Improving Seasonally Frozen Ground Monitoring Using Soil Freezing Characteristic Curve in Permittivity-Temperature Space: Sites Metadata,  
920 <https://doi.org/10.5281/ZENODO.14837416>, version Number: v1.1, 2025.
- Schimel, J. P. and Mikan, C.: Changing microbial substrate use in Arctic tundra soils through a freeze-thaw cycle, *Soil Biology and Biochemistry*, 37, 1411–1418, <https://doi.org/10.1016/j.soilbio.2004.12.011>, 2005.
- Seyfried, M. S. and Murdock, M. D.: CALIBRATION OF TIME DOMAIN REFLECTOMETRY FOR MEASUREMENT OF LIQUID WATER IN FROZEN SOILS., *Soil Science*, 161, 87–98, <https://doi.org/10.1097/00010694-199602000-00002>, 1996.
- 925 Seyfried, M. S. and Murdock, M. D.: Measurement of Soil Water Content with a 50-MHz Soil Dielectric Sensor, *Soil Science Society of America Journal*, 68, 394–403, <https://doi.org/10.2136/sssaj2004.3940>, \_eprint: <https://onlinelibrary.wiley.com/doi/pdf/10.2136/sssaj2004.3940>, 2004.
- Seyfried, M. S., Grant, L. E., Du, E., and Humes, K.: Dielectric Loss and Calibration of the Hydra Probe Soil Water Sensor, *Vadose Zone Journal*, 4, 1070–1079, <https://doi.org/10.2136/vzj2004.0148>, \_eprint: <https://onlinelibrary.wiley.com/doi/pdf/10.2136/vzj2004.0148>,  
930 2005.
- Spaans, E. J. A. and Baker, J. M.: Examining the use of time domain reflectometry for measuring liquid water content in frozen soil, *Water Resources Research*, 31, 2917–2925, <https://doi.org/10.1029/95WR02769>, 1995.

- Spaans, E. J. A. and Baker, J. M.: The Soil Freezing Characteristic: Its Measurement and Similarity to the Soil Moisture Characteristic, *Soil Science Society of America Journal*, 60, 13–19, <https://doi.org/10.2136/sssaj1996.03615995006000010005x>, 1996.
- 935 Taghipourjavi, S., Kinnard, C., and Roy, A.: Sentinel-1-Based Soil Freeze–Thaw Detection in Agro-Forested Areas: A Case Study in Southern Québec, Canada, *Remote Sensing*, 16, 1294, <https://doi.org/10.3390/rs16071294>, 2024.
- Tetlock, E., Toth, B., Berg, A., Rowlandson, T., and Ambadan, J. T.: An 11-year (2007–2017) soil moisture and precipitation dataset from the Kenaston Network in the Brightwater Creek basin, Saskatchewan, Canada, *Earth System Science Data*, 11, 787–796, <https://doi.org/10.5194/essd-11-787-2019>, publisher: Copernicus GmbH, 2019.
- 940 Tian, H., Wei, C., Wei, H., and Zhou, J.: Freezing and thawing characteristics of frozen soils: Bound water content and hysteresis phenomenon, *Cold Regions Science and Technology*, 103, 74–81, <https://doi.org/10.1016/j.coldregions.2014.03.007>, 2014.
- Tomaškovičová, S. and Ingeman-Nielsen, T.: Quantification of freeze–thaw hysteresis of unfrozen water content and electrical resistivity from time lapse measurements in the active layer and permafrost, *Permafrost and Periglacial Processes*, 35, 79–97, <https://doi.org/10.1002/ppp.2201>, 2024.
- 945 Topp, G. C., Davis, J. L., and Annan, A. P.: Electromagnetic determination of soil water content: Measurements in coaxial transmission lines, *Water Resources Research*, 16, 574–582, <https://doi.org/10.1029/WR016i003p00574>, <https://onlinelibrary.wiley.com/doi/pdf/10.1029/WR016i003p00574>, 1980.
- U.S. National Ice Center: IMS Daily Northern Hemisphere Snow and Ice Analysis at 1 km, 4 km, and 24 km Resolutions, Version 1, <https://doi.org/10.7265/N52R3PMC>, 2004.
- 950 Virtanen, P., Gommers, R., Oliphant, T. E., Haberland, M., Reddy, T., Cournapeau, D., Burovski, E., Peterson, P., Weckesser, W., Bright, J., Van Der Walt, S. J., Brett, M., Wilson, J., Millman, K. J., Mayorov, N., Nelson, A. R. J., Jones, E., Kern, R., Larson, E., Carey, C. J., Polat, , Feng, Y., Moore, E. W., VanderPlas, J., Laxalde, D., Perktold, J., Cimrman, R., Henriksen, I., Quintero, E. A., Harris, C. R., Archibald, A. M., Ribeiro, A. H., Pedregosa, F., Van Mulbregt, P., SciPy 1.0 Contributors, Vijaykumar, A., Bardelli, A. P., Rothberg, A., Hilboll, A., Kloeckner, A., Scopatz, A., Lee, A., Rokem, A., Woods, C. N., Fulton, C., Masson, C., Häggström, C., Fitzgerald, C., Nicholson, D. A., Hagen, D. R., Pasechnik, D. V., Olivetti, E., Martin, E., Wieser, E., Silva, F., Lenders, F., Wilhelm, F., Young, G., Price, G. A., Ingold, G.-L., Allen, G. E., Lee, G. R., Audren, H., Probst, I., Dietrich, J. P., Silterra, J., Webber, J. T., Slavič, J., Nothman, J., Buchner, J., Kulick, J., Schönberger, J. L., De Miranda Cardoso, J. V., Reimer, J., Harrington, J., Rodríguez, J. L. C., Nunez-Iglesias, J., Kuczynski, J., Tritz, K., Thoma, M., Newville, M., Kümmerer, M., Bolingbroke, M., Tartre, M., Pak, M., Smith, N. J., Nowaczyk, N., Shebanov, N., Pavlyk, O., Brodtkorb, P. A., Lee, P., McGibbon, R. T., Feldbauer, R., Lewis, S., Tygier, S., Sievert, S., Vigna, S., Peterson, S., More, 955 S., Pudlik, T., Oshima, T., Pingel, T. J., Robitaille, T. P., Spura, T., Jones, T. R., Cera, T., Leslie, T., Zito, T., Krauss, T., Upadhyay, U., Halchenko, Y. O., and Vázquez-Baeza, Y.: SciPy 1.0: fundamental algorithms for scientific computing in Python, *Nature Methods*, 17, 261–272, <https://doi.org/10.1038/s41592-019-0686-2>, 2020.
- von Hippel, A. R.: *Dielectrics and Waves*, The MIT Press, ISBN 978-0-262-72003-8, 1966.
- Watanabe, K. and Osada, Y.: Simultaneous measurement of unfrozen water content and hydraulic conductivity of partially frozen soil near 0 965 °C, *Cold Regions Science and Technology*, 142, 79–84, <https://doi.org/10.1016/j.coldregions.2017.08.002>, 2017.
- Williams, P. J. and Smith, M. W.: *The Frozen Earth: Fundamentals of Geocryology*, Cambridge University Press, 1 edn., ISBN 978-0-521-36534-5 978-0-521-42423-3 978-0-511-56443-7, <https://doi.org/10.1017/CBO9780511564437>, 1989.
- Wu, Y., Nakagawa, S., Kneafsey, T. J., Dafflon, B., and Hubbard, S.: Electrical and seismic response of saline permafrost soil during freeze - Thaw transition, *Journal of Applied Geophysics*, 146, 16–26, <https://doi.org/10.1016/j.jappgeo.2017.08.008>, 2017.

- 970 Yoshikawa, K. and Overduin, P. P.: Comparing unfrozen water content measurements of frozen soil using recently developed commercial sensors, *Cold Regions Science and Technology*, 42, 250–256, <https://doi.org/10.1016/j.coldregions.2005.03.001>, 2005.
- Zhang, M., Zhang, X., Lu, J., Pei, W., and Wang, C.: Analysis of volumetric unfrozen water contents in freezing soils, *Experimental Heat Transfer*, 32, 426–438, <https://doi.org/10.1080/08916152.2018.1535528>, 2019.
- Zhang, T.: Influence of the seasonal snow cover on the ground thermal regime: An overview, *Reviews of Geophysics*, 43, 2004RG000 157, 975 <https://doi.org/10.1029/2004RG000157>, 2005.
- Zhang, T. and Armstrong, R. L.: Soil freeze/thaw cycles over snow-free land detected by passive microwave remote sensing, *Geophysical Research Letters*, 28, 763–766, <https://doi.org/10.1029/2000GL011952>, 2001.
- Zhang, T., Barry, R. G., Knowles, K., Ling, F., and Armstrong, R.: Distribution of seasonally and perennially frozen ground in the Northern Hemisphere, in: M. Phillips et al., editors, *Proceedings of the 8th International Conference on Permafrost*, Zürich, Switzerland. 21–25 July 980 2003, pp. 1289–1294, A.A. Balkema, Rotterdam, the Netherlands, 2003.
- Zhou, X., Zhou, J., Kinzelbach, W., and Stauffer, F.: Simultaneous measurement of unfrozen water content and ice content in frozen soil using gamma ray attenuation and TDR, *Water Resources Research*, 50, 9630–9655, <https://doi.org/10.1002/2014WR015640>, 2014.